Experimental and Mechanistic Study of Stabilized Dry CO_2 Foam Using Polyelectrolyte Complex Nanoparticles Compatible with Produced Water to Improve Hydraulic Fracturing Performance

*[1]Hooman Hosseini, [2]Jyun Syung Tsau, [2]Karen Shafer-Peltier, [3, 4]Craig Marshall, [5]Qiang Ye, [1]Reza Barati Ghahfarokhi**

[1]Department of Chemical and Petroleum Engineering, University of Kansas, Lawrence, Kansas 66045, USA

[2]Tertiary Oil Recovery Program, University of Kansas, Lawrence, Kansas 66045, USA

[3]Department of Geology, University of Kansas, Lawrence, Kansas 66045, USA

[4]Department of Chemistry, University of Kansas, Lawrence, Kansas 66045, USA

[5]Institute for Bioengineering Research, University of Kansas, Lawrence, Kansas 66045, USA

Correspondence to: Reza Barati Ghahfarokhi (E-mail: rezab@ku.edu)

ABSTRACT:

The amount of fresh water used in hydraulic fracturing can be significantly reduced by employing produced water compatible supercritical CO_2 ($scCO_2$) foams. Foams generated using surfactants only have suffered from long term stability issues resulting in low viscosity and proppant carrying problems. In this work foam lamella stabilization with polyelectrolyte complex nanoparticles (PECNP) and wormlike micelles is investigated. Electrostatic interactions are studied as the defining factors improving the hydraulic fracturing performance using the PECNP system prepared in produced water.

Two oppositely charged polyelectrolytes are investigated to generate a more stable lamellae between the aqueous phase and the $scCO_2$ while degrading in the presence of crude oil. The generated dry foam system is used as a hydraulic fracturing fluid in tight shale formation. The strong compatibility of the synthesized polyelectrolyte complex nanoparticles (PECNP) with zwitterionic surfactants prepared in highly concentrated brine in the form of wormlike micelles (WLMs) above Critical Micelle Concentration (CMC) helps develop a highly viscous, dry foam capable of using produced water as its external phase. This foam system improves fracture propagation, proppant transport fracture cleanup compared to the base case foam system with no PECNP. The formation of PEC-surfactant nanoparticles was verified via zeta potential, particle size analysis, and transmission electron microscopy (TEM) where the underlying mechanism was identified as electrostatic rearrangement of WLMs along the PECNP's perimeter or formation of electrostatically bonded micelles with nanoparticle to create a new enhanced nanoparticle. A Raman spectroscopic model was developed to understand the PECNP-surfactant spectra and subsequent spectroscopic and hence structural changes associated with complexation. Enhanced bulk viscosity and improved foam quality as a result of complexation at the interface was identified

with rheometry in addition to sand pack experiments with PECNP-surfactant ratios of 1:9 and 4:6, in 33.3 kppm and 66.7 kppm salinity brine systems, respectively. Enhancement in the shear thinning and clean-up efficiency of the fracturing fluid was observed. Formation damage was controlled by the newly introduced mixtures as fluid loss volume decreased across the tight Kentucky sandstone cores by up to 78% and 35% for $scCO_2$ foams made with PECNP-WLMs in 33.3 and 66.7 kppm salinity brine, respectively. The produced water compatibility and reduction of water disposal presented the prospect of environmentally friendly $scCO_2$ foams for hydraulic fracturing of unconventional reservoirs.

KEYWORDS: "Polyelectrolyte Complex Nanoparticles", "Hydraulic Fracturing", "Zwitterionic Surfactants", "Raman spectroscopy", "CO_2 foam", "Produced Water".

1. INTRODUCTION

Unconventional oil and gas resources are increasingly demanded due to rapid climb in energy consumption, technological advances and depletion of easy-to-produce conventional resources. Prospects of unconventional technologies such as hydraulic fracturing and directional drilling represent a future energy portfolio and a game changing production technique that outperforms the conventional drilling methods to stimulate shale and tight hydrocarbon reservoirs [1,2]. First introduced into commercial practice in 1947 and effectively combined with horizontal drilling in the late 1990s, hydraulic fracturing is the most enduring technology ever developed to enhance gas and petroleum liquid production from low permeability formations (permeability less than 1 mD and below 15% porosity) [2–4]. Upon fracture creation, the pressurized fluid carrying the proppant is injected to the fractured reservoir to keep the fracture propped open and to let the hydrocarbons flow from the fractures to the producing well and surface [5]. Hydraulically fractured oil and gas wells are typically located near drinking water resources, thus, the water cycle

process could influence the quality of drinking water in different stages from water withdrawal and chemical mixing of fracturing fluids, to water disposal and reuse of produced water [6]. The impact could leave negative consequences on areas of lower water availability, in terms of groundwater and surface water quality [7], spill management [8], fracturing pad leakage [9], high cost of water disposal [4], excessive water withdrawal and water contamination [6]. As large amount of fresh water, ground water or surface water, about 5.7 million L between 2011 to 2013 [6], are used for hydraulic fracturing, a water management strategy within the fracturing process can reduce the frequency of severity of impacts on earthquakes and drinking water and expenses associated to water treatments.

Low initial water saturation in majority of tight shales makes water blocking-caused by injection of water-based fluids-a more effective mechanism in decreasing permeability [10,11]. Water trap due to capillary retention [10], costly pressure drawdown to recover the water [12] and abundance of water-sensitive formations [13] highlight the importance of waterless fracturing techniques that are capable of carrying proppants [4], while maintaining the fracture conductivity using the least amount of water.

The development of ”water-less” fracturing fluids in the form of foams containing stabilizers such as nanoparticle and surfactants introduces a viable solution for water sensitive formations [14]. Foams, as predominant dispersion of gas in liquids, are promising candidates to address the issue with variable amount of water and at least one compressible component such as CO_2 or N_2 within the composition [3] CO_2 is abundant, nonflammable and non-toxic and CO_2 emission into atmosphere prompts the efforts to effective capture utilization and storage (CCUS) [15,16]. Low density and viscosity of CO_2 enhances the propagation in low permeability reservoirs, however, there exist issues reported with ice formation [17], challenges in storage [18] and filtration of liquid

CO_2-based fracturing fluid [4]. CO_2 storage in dense phase is performed in supercritical state where fluid is held above the critical point (31.1°C and 7.4MPa) [19]. $scCO_2$ offers properties such as enhanced rates, improved mass transfer and increased selectivity [20] in between the CO_2 gas (diffusivity) and CO_2 liquid (density), which introduces a prime candidate for fracturing [21,22].

To enhance the compatibility of $scCO_2$ with water phase, a variety of methods were proposed. The presence of adsorbed surfactant layers stabilize the lamellae between the $scCO_2$ and the aqueous phase [23] taking advantage of electrostatic repulsion between the two faces of lamellae [24]. Likewise, increasing the surfactant concentration under the influence of electrolyte concentration would help with formation of a long-range electrostatically ordered microstructure on the thin liquid films and the bulk of the lamellae to inhibit foam film drainage (stratification) [25] Formation of viscoelastic lamella stabilizes the gas-in-water foams by suppressing the gravity drainage, lamella thinning and eventually Ostwald ripening [22].

Nanoparticles [5] were found to overcome the challenges associated to surfactant adsorption on reservoir rocks [4], thermal conductivity [26], fluid loss [27], water invasion [28], fluid propagation in porous media [5,29] and pore throat plugging [30] to achieve proper fracture width and height [4]. Polyelectrolytes are widely used charged polymers compatible with aqueous solutions while being useful for adsorption [31], ionic conduction [32], ultrafiltration [33] and controlled release [34]. Branched polyethylenimine (PEI) with different types of cationic amine functionality is capable of polyelectrolyte complex nanoparticles (PECNP) formation in electrostatic complexation with dextran sulfate (DS) comprising anionic sulfonate functionality in adjusted pH medium [3]. In this work, electrostatic interaction between polyelectrolyte complex nanoparticles with entangled wormlike micelles (WLM) of viscoelastic surfactant (VES) is investigated to eliminate fluid loss issues, to improve the viscosity of VES-based fluids and to

enhance the proppant suspension capabilities. To understand the underlying mechanism of synergistic electrostatistic complexation between surfactant and polymer in the bulk lamella mixture, Raman spectroscopy was employed. In order to tailor ionic activity of surfactants and to decline the rate of lamellae drainage, polyelectrolyte complex nanoparticles were developed by our group for both Enhanced Oil Recovery (EOR), reservoir treatment and hydraulic fracturing applications [3,34–38]. Interactions between the polyelectrolytes and oppositely charged sites on the surfactant creates a variety of different colloidal systems with liquid crystalline-like mesostructured and long-range order on nanometer scale. The supercharged and stable nano aggregates in high salinity produced water are capable of stabilizing CO_2-water interface to resist against the shear around the wellbore, to carry the proppants to the fracture and to reduce leak-off in tight formations. The stability of optimized proportions of PECNP-Surfactant in high salinity brine improves the viscosity, elasticity and fracture conductivity, whereas, rapid oil instability is offered through oil spreading through the lamella to break and release the proppants.

2. MATERIALS AND METHODS

2.1. Material synthesis and preparation. High salinity brine was synthesized according to procedure introduced by Hosseini et al [3]. The Mississippian Limestone Play (MLP) recipe contains aqueous solution of more than 202,848 ppm total dissolved solids consisting of $CaCl_2.2H_2O$ (Fisher Chemical, Certified ACS), $MgCl_2.6H_2O$ (Fisher Chemical, Certified ACS, Crystalline), $SrCl_2.6H_2O$ (Fisher Science Education, Lab Grade), Na_2SO_4 (Fisher Chemical, Certified ACS, Granular) NaCl (Fisher Chemical, Certified ACS, Crystalline) and KCl (Fisher Chemical, Potassium chloride for calomel cells, Crystalline). The salts were added to reverse osmosis and deionized water (RO- DI- water). The salt type and concentration in MLP brine are shown in Table 1. The highly concentrated brine synthesized according to laboratorial recipe

adopted from original MLP recipe (202,848 ppm, ~200,000 ppm) was then diluted to 66,666 ppm (3X) and sea-water level 33,333 ppm (6X) nominal concentrations.

Table 1.Mississippian Limestone Play (MLP) brine composition (original and laboratorial concentrations)

MLP	Elements	Ca	Mg	Na	K	Cl	Sr,Fe,Mn,SO_4,etc	Total
Nominal Concentration	Concentration (mg/L)	12,780.4	2,601.1	64,779.4	374.9	12,630	1,482.6	202,648.4
Synthesized MLP	Salt	NaCl	Na_2SO_4	KCl	$MgCl_2.6H_2O$	$SrCl_2.6H_2O$	$CaCl_2.2H_2O$	Total
Lab Concentration	Concentration (mg/L)	163,661	1,224	715	21,759	1,535	46,886	235,782

Zwitterionic surfactant HDP-0761-12-2AM was provided by Harcros Chemicals Inc. The surfactant structure was designed for optimum ionic activity in form of short chain aliphatic molecules with positive amine and negative sulfonate functional groups. The main ingredients in the form of solvent and additive to the surfactant solutions are listed in Table 2 (provided by Harcros).

Table 2. Solvent and additives in HDP-0761-12-2AM surfactant provided by Harcros

Chemical Name	CAS number	%
Water	7732-18-5	60 -< 70
Sodium Chloride	7647-14-5	5 -< 10
3-chloro-1,2-Propanediol	96-24-2	< 0.2
Other components below reportable levels	-	30 -< 40

The surfactant was dissolved in 33.3 kppm and 66.7 kppm brines to form 1 w/w% reference solutions. Polyelectrolyte complex nanoparticles (PECNP) were prepared according to the procedure developed by Barati and co-workers [3,36,37]. Branched Polyethylenimine (PEI) was obtained from Sigma Aldrich with an average molecular weight of 25,000, 1.03 g/mL density at 25 °C and corresponding viscosity ranging between 13,000 cP to 18000 cP at 50 °C. Dextran Sulfate (DS) was provided from Sigma Aldrich with 500,000 molecular weight. PEI and DS were separately dissolved in high salinity brines with 1 w/w% and the pH for PEI solution was lowered to 8.5 by addition of 6N HCl [3,37] (Figure S1 in Supporting Information-SI). The solution of 1

w/w% DS in high salinity brine was prepared and PEI and DS solutions were mixed accordingly. The mixing ratio of PEI to DS, to the diluting brine solution (PEI:DS:Brine) was chosen to be 3:1:0.1 to make positively charged nanoparticles. This ratio was developed based on previous observations with zeta potential and particle size measurements [35,36]. The nanoparticle solution was mixed with surfactant solutions (1 w/w %) in both 33.3 kppm and 66.7 kppm brine systems for 20 minutes to form the PECNP/surfactant complexation with different mixing ratios of PECNP:surfactant (1:9, 2:8, 3:7, and 4:6). The concentration of the surfactant remains constant in mixing with nanoparticles (1w/w %). The foaming solution was later mixed with Air (50 v/v %) or $scCO_2$ (90 v/v %) in inline mixers at 40 °C to form the actual foam.

2.2. Fourier Transform-Infrared (FT-IR) spectroscopy. The chemical functional groups on the surfactant molecules were examined with a Spectrum 400 FT-IR spectrometer (Perkin Elmer, Waltham, MA) equipped with two temperature stabilized deuterated triglycine sulphate detectors. A small aliquot of liquid sample was deposited onto the diamond crystal top plate of an attenuated total reflection (ATR) accessory (GladiATR, Pike Technologies, Madision, WI). Sixty scans were co-added over the range of 4000-650 cm^{-1} with a spectral resolution of 4 cm^{-1}. Air was taken as the reference for the background before each sample. After acquisition of each spectrum, the ATR plate was cleaned in situ by cleaning it with ethanol solution three times, and allowing it to dry. No residue from the previous sample was observed in subsequent background spectra and when compared it to the previous background spectra. Also an atmospheric correction routine is performed for CO_2/H_2O suppression by the Spectrum software (PerkinElmer, Waltham, MA). The results are shown in Figure S2.

2.3. Dynamic light scattering. The hydrodynamic diameter of ionic particles was measured by dynamic light scattering measurement, through the average of three readings using a NanoBrook

Omni Particle sizer and zeta potential analyzer by Brookhaven Instruments. pH of colloidal solutions, density and viscosity of each sample as well as mean particle diameter were employed for determining the zeta potential. For the zeta potential measurements, the samples were diluted 20 times in background electrolyte of 1mM KCl where the average of three readings were considered for analysis on the NanoBrook Omni. The standard 35 mV red diode laser with nominal 640 nm wavelength was employed to detect the size range, size distribution and electrophoretic mobility using the Smoluchowski model.

2.4. The air-foam stability measurements. Experimental setup was designed to quantify bulk foam height as a function of time to determine the aqueous foam stability. The predetermined amount (10 mL) of foaming solution comprising different proportions of PECNP to surfactant (PECNP:Surfactant of 1:9, 2:8, and 3:7) was transferred to 20 mL vials for primary foam decay analysis. The sealed and scaled vial containing the 50 % mixture with air was heavily agitated for almost 30 times for perfect mixing of air and liquid. The scaled vial was placed and kept in an oven with a constant temperature of 40 ºC (Figure S3 in SI). A camera was set inside the oven and the air foam height in the vials was recorded every minute.

2.5. Interfacial tension analysis. $scCO_2$ interfacial tension in high salinity brine containing surfactants and PECNP was measured according to axisymmetric drop shape analysis of pendant drop by a tensiometer at pressures and temperatures in which CO_2 is in supercritical conditions. The $scCO_2$ bubble is formed on the tip of stainless steel capillary in high pressure chamber (1330 psi) filled with PECNP-surfactant solution while isothermal temperature of 40 °C was maintained by applying thermal jackets around the pipes and chamber. The DROPimage software and high-resolution camera were employed to measure the surface tension for each bubble in dynamic mode for 1 h. A minimum of three runs for each sample was recorded. Schematic of the employed

tensiometer in this analysis is provided in Figure 1. The droplet area was determined by analyzing the droplet profile using a camera coupled with image analyzer software (DROPimage).

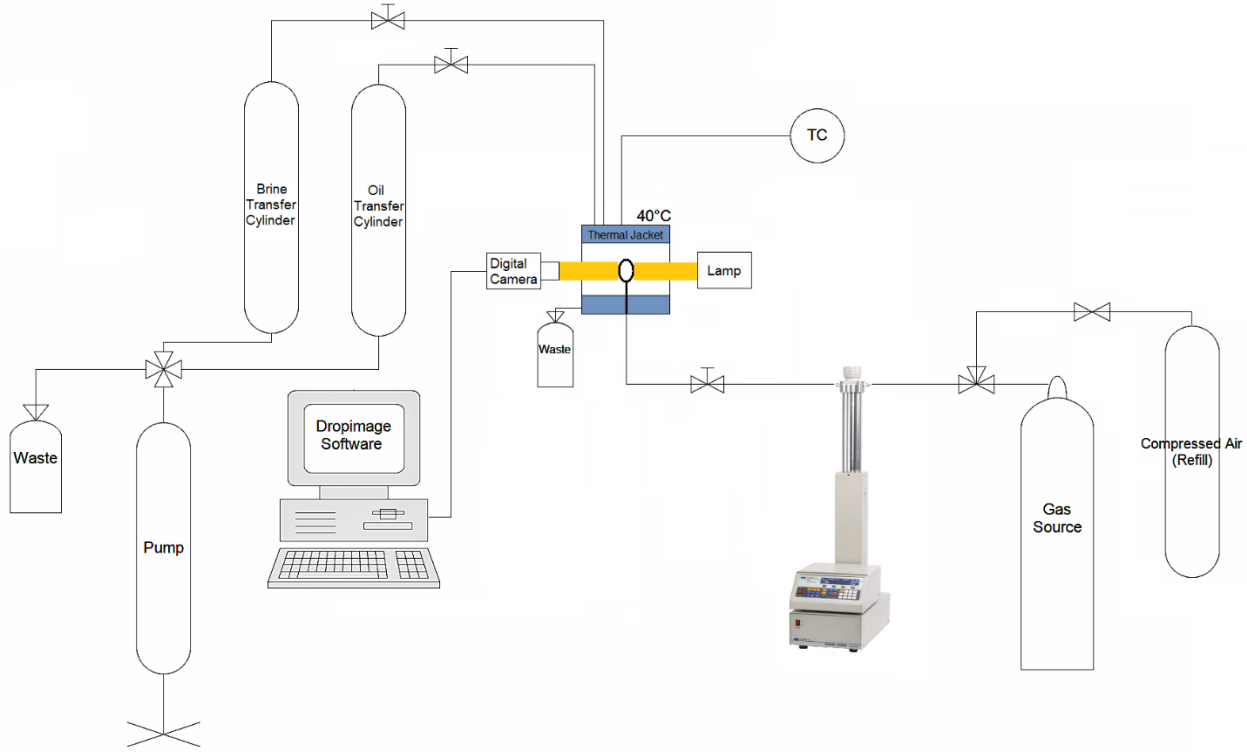

Figure 1.Process flow diagram for interfacial tension analysis setup.

Critical micelle concentration (CMC) was determined with different concentrations of surfactant dissolved in high salinity brines and the corresponding interfacial tension was estimated accordingly. Dilatational elasticity was estimated according to a ramp-type perturbation approach previously presented by Tewes and coworkers [39]. The variation of interfacial pressure after compression of equilibrated surface layer of pendant drop is correlated to surface area variation as a result of mechanical strain to estimate the equilibrium surface dilatational elasticity [39,40]:

(1) $$\Delta\pi_e = E_e \frac{U_b t}{A_i}$$

where A_i is surface area prior to applying the mechanical strain. The non-equilibrium portion is also calculated based upon dissipation of accumulated energy during compression and relaxation [39].

(2) $$\Delta\pi_{ne} = \frac{E_{ne}U_b t}{A_i}\left(1 - e^{-\frac{t}{\tau}}\right)$$

Details of calculations are found in the SI section (Figure S4).

2.6. Rheological measurements. Oscillatory shear stability of bulk foam is examined through stress-controlled rotational measurements using an Anton-Paar MCR 302 rheometer. The temperature was controlled by a water-circulating bath (6 to 40 °C). The setup utilized feed cylinders, pumps, circulating coolers and thermal isolators (Figure 2). A Couette geometry module was used in a pressure cell to study the viscoelastic behavior of $scCO_2$ foam. Constant (2000 s^{-1}) and variable shear rates (2000 s^{-1} to 100 s^{-1}) were used for static (stagnant foam in the cell) and dynamic (continues flow of foam in the cell) measurements at 40 °C and 1,350 psi. The detailed procedure is introduced in the SI.

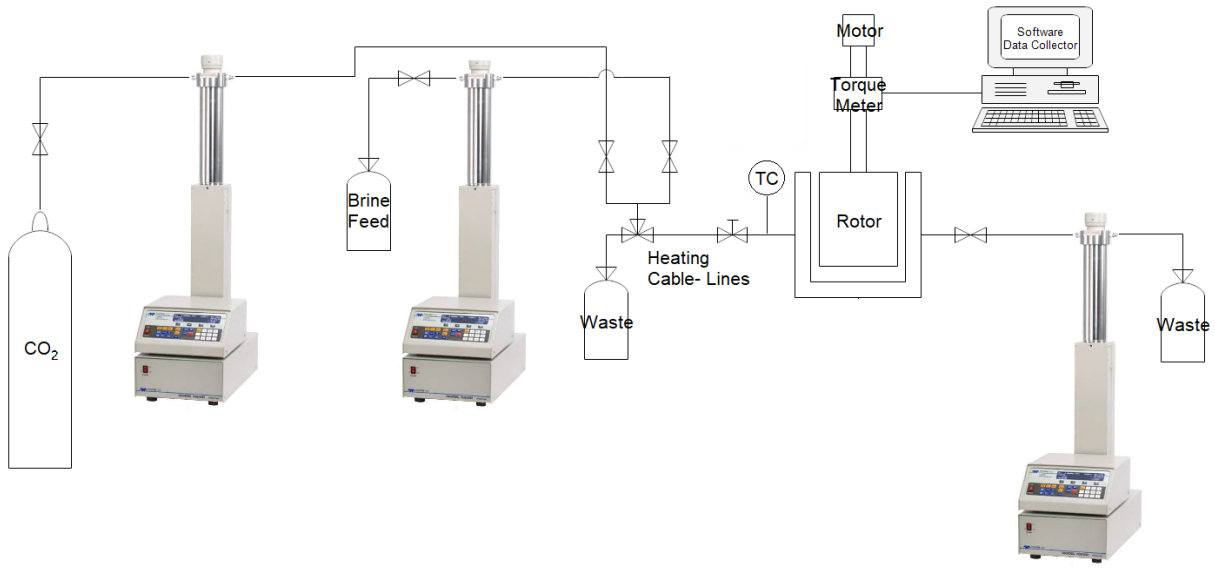

Figure 2. Process flow diagram for rheometer setup

2.7. Raman spectroscopy. Raman spectra of lyophilized powders were determined by using a LabRAM ARAMIS Raman spectrometer (LabRAM HORIBA Jobin Yvon, Edison, NJ) with a HeNe laser ($\lambda = 633$ nm, power = 17 mW) as an excitation source. The instrument conditions were: 200 μm confocal hole, 150 μm wide entrance slit, 600 g/mm grating, and 50X long working distance objective Olympus lens. Data acquisition was performed using LabSPEC 5 (HORIBA Jobin Yvon). The samples were mounted in a computer-controlled, high-precision x–y stage. Spectra were acquired over a range of 700–2400 cm^{-1} with 60 s exposure time and 10 times accumulation.

The acquired Raman spectra were processed using Matlab (the MathWorks, Inc. Natick MA, USA) to smooth the curves (through binning adjacent data points), to remove digital noise (through binning adjacent data points) and to remove the fluorescence background (by subtracting a fifth order polynomial fit to the original spectrum). Furthermore, contributions to the spectra from cosmic rays were removed manually when appropriate. The spectra of mixtures of PECNP and surfactant (1:9 ratio) were fit with average surfactant and PECNP spectra using least-squares fitting in a manner similar to the method described by Shafer-Peltier for modeling of biological Raman spectra [41].

Spectra of dextran sulfate and polyethylenimine were also collected in the same manner to aid in data interpretation and peak assignment but were not included in the model. Vectors representing each fit were created using the MATLAB polyval function and residuals of each fit were determined. An average of three to four spectra were then used (except in the case of the PECNP:Surfactant complex spectra) for further analysis.

2.8. Transmission Electron Microscopy (TEM). 5 μl of a solution of PECNP and PECNP-surfactant mixture was placed onto a 300 mesh Lacey carbon copper grid (EMS LC 300 Cu),

respectively, for 1 minute and blotted twice with a filter paper. The 300 mesh copper grid with PECNP and PECNP-surfactant mixture was examined using a 200 kV FEI Tecnai F20 XT field emission transmission electron microscope at an electron acceleration voltage of 160 kV. TEM images were captured using a normative and standardized electron dose on eucentric specimen stage and a constant defocus value from the carbon-coated surfaces. Images were randomly acquired in a size of (1024 x1024) pixel resolution at 10 different locations within the grid.

2.9. View cell, dynamic fluid loss and sand pack measurements. The $scCO_2$ foam stability, core fluid loss properties and fracture clean up performance were examined via a high pressure-high temperature foam flooding apparatus utilized with shear loop mixer, sapphire view cell, dynamic fluid loss and sand pack modules. The schematic of the system is presented in Figure 3.

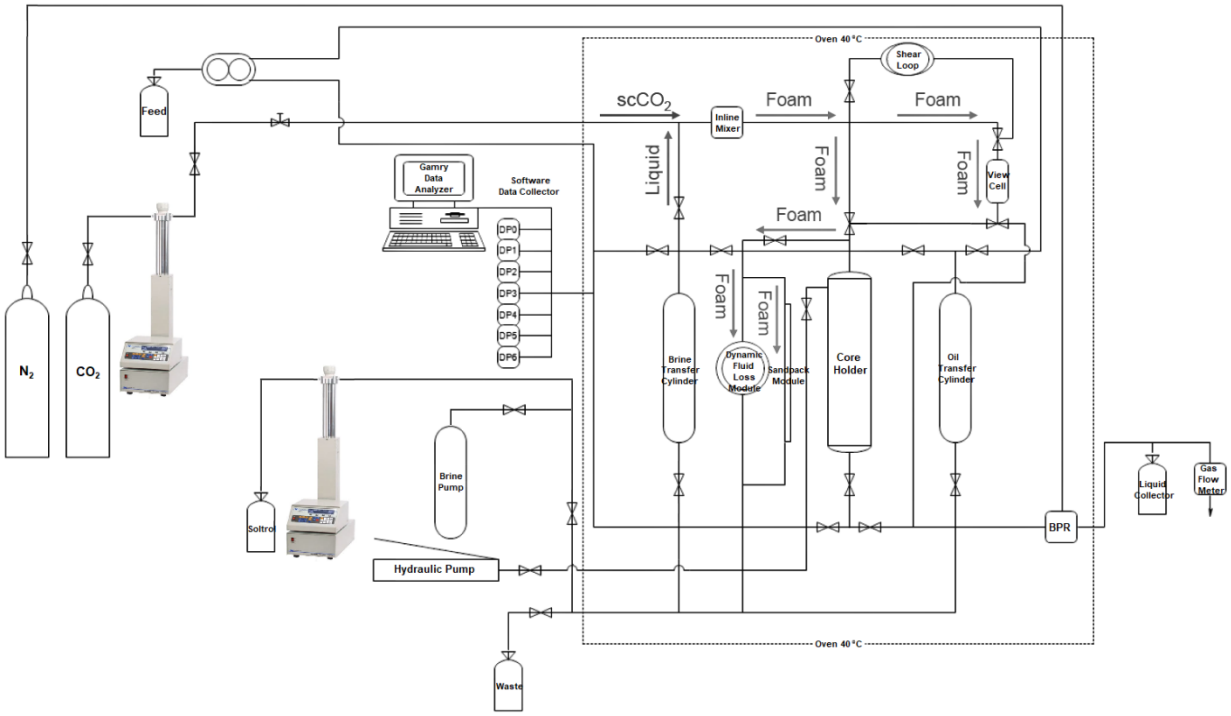

Figure 3. Flow diagram for high pressure, high temperature CO_2 foam flooding setup with view cell foam stability module, fluid loss and sand pack modules. Pathways A, B and C represent the foam flow through view cell, dynamic fluid loss and sand pack modules

The foam is generated with in-line mixing of $scCO_2$ foam (40°C, 1350 psi) and the aqueous solution (surfactant or PECNP:Surfactant solutions) prepared in 33.3 kppm and 66.7 kppm high salinity brine with different proportions of PECNP:Surfactant (1:9, 2:8, 3:7, and 6:4, with 0:10 being the surfactant solution itself). The foaming liquid is mixed with $scCO_2$ and the components are directed toward the Swagelok inline mixer with 7 μm pore size. The generated foam is then directed to the view cell to measure the foam stability and foam textural properties. A GoPro camera was set to record the foam height on every minute and a Unimake camera microscope utilized with CMOS image sensor was used to observe the foam microstructure. After the foam was established in the view cell, oil was immediately introduced to the view cell to evaluate the stability of the of $scCO_2$ foam in the presence of crude oil. The generated foam could also be directed to the fluid loss module embedded low with a permeability Kentucky sandstone (Table 3) sitting perpendicular to fluid flow to measure the ability of fracturing fluid to prevent the leak-off in the tight formation.

Table 3. Physical properties for Kentucky sandstone core, data provided by Kocurek Industries.

Core	Gas Permeability	Brine Permeability	Porosity	UCS Strength
Kentucky Sandstone Core	1 to 5 mD	0.18 mD	14%	8000 psi

The volume of lost gas and liquid through the core and their corresponding fluid loss coefficient were measured according to equation [42]:

$$V_L = C_w\sqrt{t} + S_P \quad (3)$$

Where V_L is the total fluid loss volume (gas and liquid), C_w is fluid loss coefficient (wall-building coefficient) and S_p is the volume leaked off before any filtration occurred.

The mixture of $scCO_2$ and foaming solution can also be directed to a pack of low density, 20/40 mesh size, ceramic proppant (CARBOECONOPROP provided by CARBO CERMAICS INC.) [43] saturated with high salinity brine (predetermined pore volume) and MLP crude oil. The

sequence for sand pack experiment includes primary brine flood to measure the initial pack permeability, oil flood for pack saturation, foam flood for pack clean-up and secondary brine flood for final pack permeability after clean-up. The pressure difference across the dynamic fluid loss and sand pack is monitored with Validyne pressure transducers linked to Gamry data analyzer. The system contains the left transfer cylinder filled with foaming solution and right transfer cylinder filled with MLP crude oil with properties provided in Table 4.

Table 4. MLP crude oil properties

Oil	Viscosity	Density
Mississippian crude oil	3.88 cP	0.83 g/cm^3

3. RESULTS

3.1. Particle size and zeta potential measurements. The particle size and zeta potential values for variety of PECNP to surfactant proportions (1:9, 2:8, 3:7 and 4:6) in 33.3 kppm and 66.7 kppm brine solutions are presented in Figure 4.

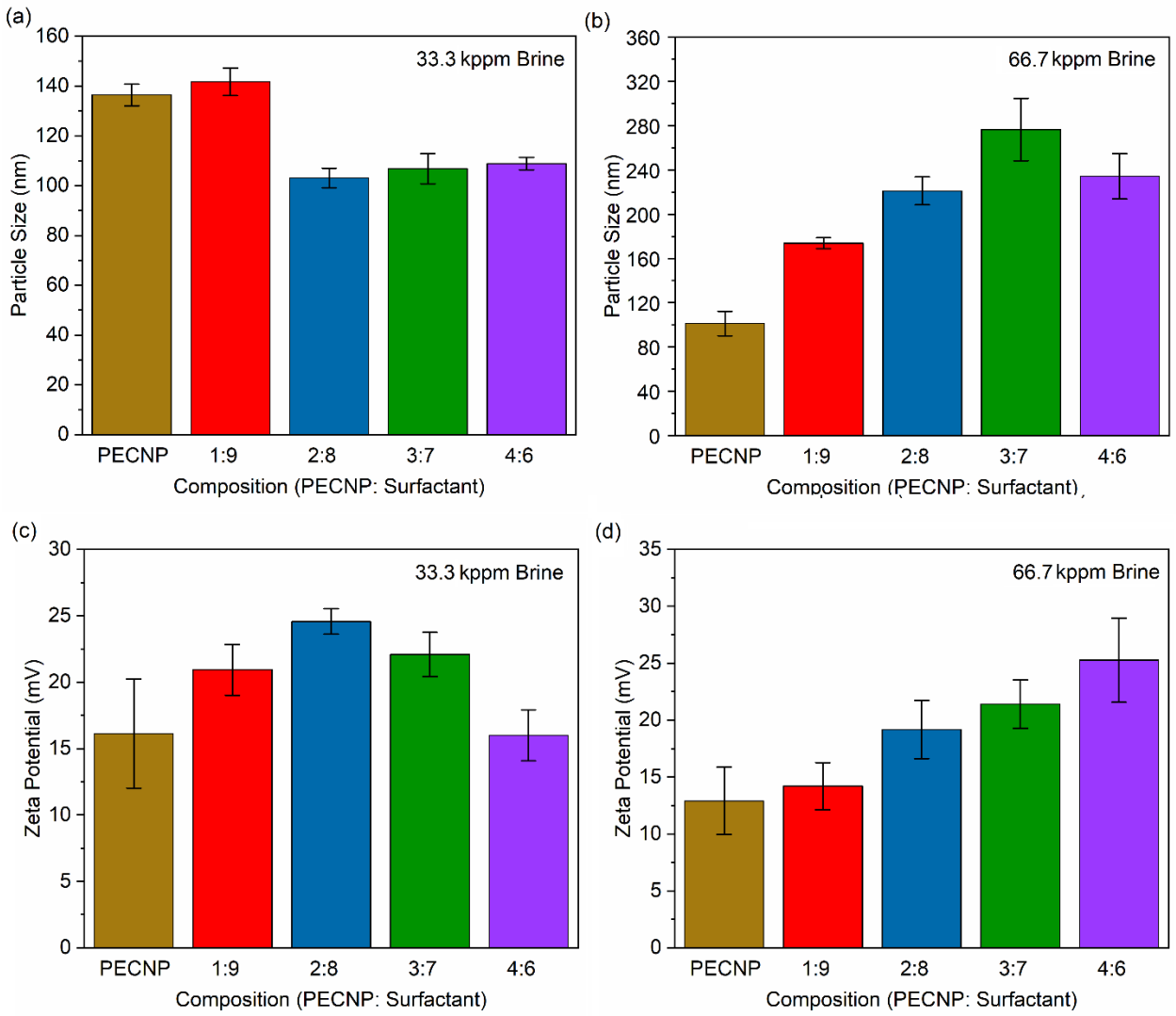

Figure 4. Particle size and zeta potential measurements for PECNP and different proportions of PECNP to surfactant in 33.3 kppm and 66.6 kppm brine systems

For 33.3 kppm brine system, PEI and DS form PECNPs within the size range of 132 to 140 nm with an average zeta potential of +16 mV (Figure 4a,c) due to an excess of amine functional groups on the outer layer of the nano-aggregates resulting in a positive charge (PEI:DS 3:1). Addition of nanoparticles with the lowest proportion (1:9) to the surfactant solution enhances the average particulate size, preventing the fluid loss of the final mixture by bridging the pores on the

surface of the rock matrix [44]. Nevertheless, further addition of PECNP lowers the average particle size due to precipitation and charge instability (Figure 4a). Accordingly, PECNP:surfactant with the 1:9 and 2:8 ratios represent the highest positive zeta potential on the surface of nanoaggregates and no further stable charge accumulations were observed for higher proportions of PECNP in the 33.3 kppm brine system due toionic and charge imbalances on the PECNP and surfactant coagulates, allowing electrostatic attractions of opposite charges and electrostatic instabilities. Considering the combined effect of particle size and charges, the 1:9 ratio for PECNP:Surfactant is the prime candidate to stabilize the CO_2 - water lamella and prevents the fluid loss in 33.3 kppm brine mixtures.

Particle size and potential for ionic mixtures at 66.7 kppm system are represented in Figure 4b, d. Addition of PECNP to WLMs directly enhances the particle size and positive potential. Higher salinity enhances the hydrophilicity of formed nanoparticles and it accelerates the aggregation of PECNPs, and PECNP-surfactant due to weakening of electrostatic repulsions and higher concentration of divalent ions. As previously reported, the stronger adsorption of nanoparticles on the lamellae and formation of an electrostatic dense layer in the lamella results in particles with larger zeta potentials [30,45], therefore, ratios of 3:7 and 4:6 result in optimal size and surface charge in the 66.7 kppm high salinity brine and the stable quasi colloidal particles of PECNP and surfactants (WLMs) can withstand harsh condition of high salinity brine.

3.2. Foam stability measurement. For initial stage of stability measurements the foaming mixture was mixed with air as shown in Figure 5. The foam height was measured with respect to time.

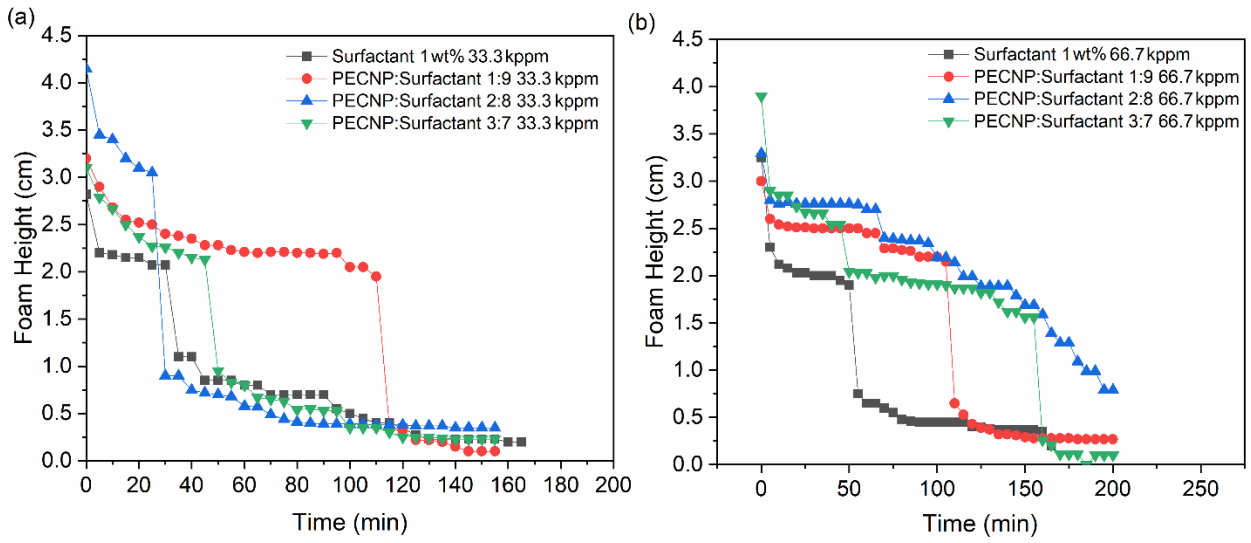

Figure 5. Preliminary foam stability test for different ratios of PECNP to Surfactant mixed with air for two different brine concentrations (a) 33.3 kppm and (b) 66.7 kppm

Zhang and coworkers reported adsorption and self-assembly of micelles above CMC at the air-water interface for ionic surfactants forming surface segregation with hydrophobic and hydrophilic regions so repartitioning around the gas-liquid interface [46]. Surfactant-water solubility and nanoparticle compatibility to the ionic interface helped to create relative stability as the resulting foam remains stable for at least 100 min when optimum concentrations of micelles and nanoparticles exist.

Actual foam stability measurement were performed on $scCO_2$ mixture with PECNP-surfactant in high salinity brines. Figure 6 illustrates the foam stability measurements and the actual foam formation and degradation inside the sapphire view cell (Figure 6c). Fine-textured and homogenous cellular structures with significant microcellular texture (~400 to 700 µm) were formed with different ratios of PECNP to surfactant solution. Uniform bubble size and distribution was achieved with 1:9 and 4:6 portions of PECNP to surfactant (Figure 6d).

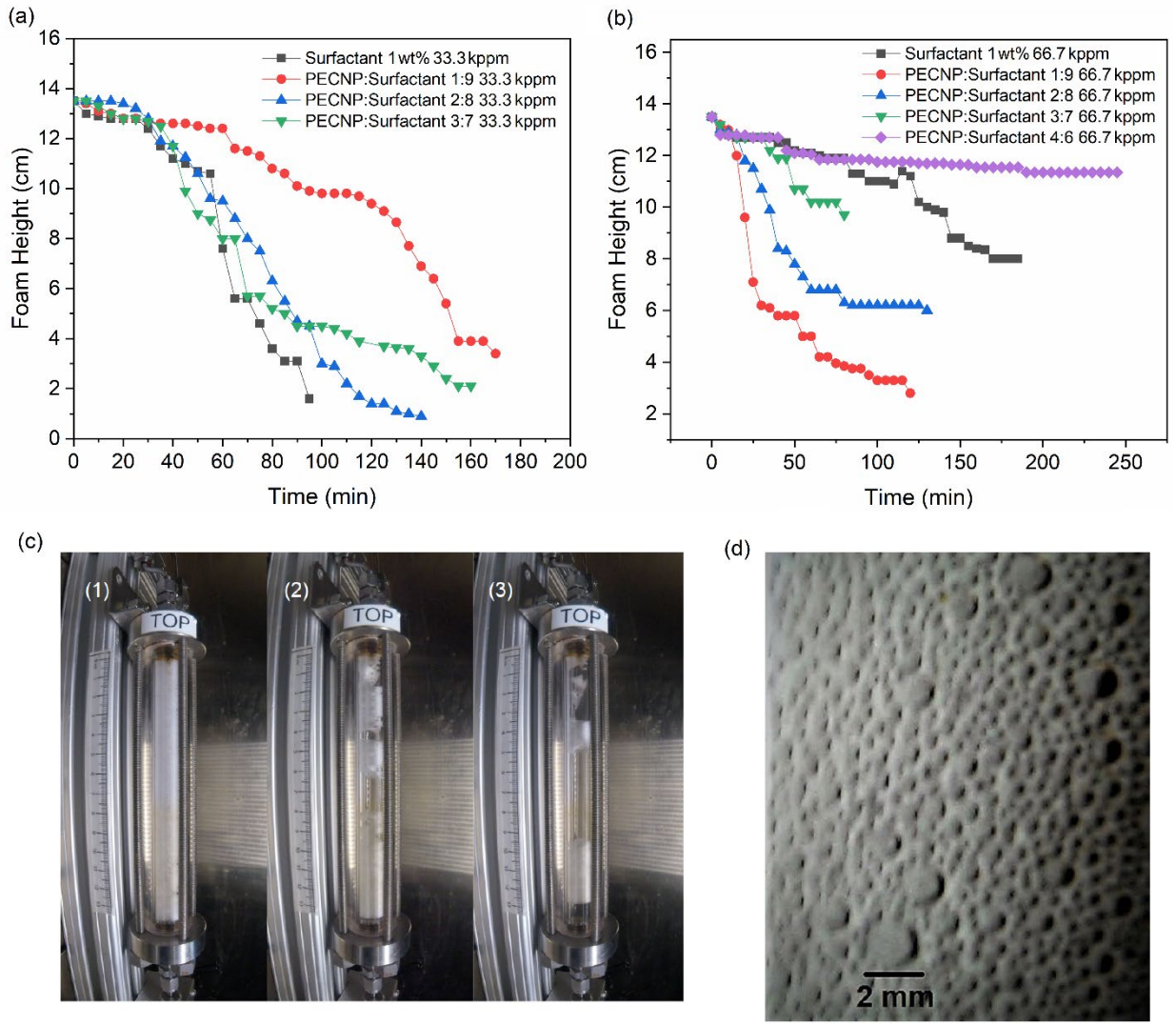

Figure 6. Foam stability measurements for $scCO_2$ foam made with variety of PECNP-surfactant mixtures in (a) 33.3 kppm brine solutions. (b) 66.7 kppm brine solutions (c-1) Foam generation and isolation in the view cell (c-2) foam drainage progress (c-3) Total foam disappearance and breakage (d) foam microstructural view inside the view cell for PECNP:Surfactant 1:9 in 33.3 kppm brine.

Likewise, the longest-lived foam belongs to 1:9 and 4:6 ratios in the 33.3 kppm and the 66.7 kppm brines, respectively, as foam preserves the cellular structure for at least 2 h in the view cell in these scenarios. The foam half-decay time for different systems are presented in Table 5. The half-decay time for PECNP-surfactant (with 1:9 ratio in 33.3 kppm brine) is more than twice that of 1 wt% surfactant mixed with $scCO_2$. The half-life shortens when a higher portion of

nanoparticle is used due to lower electrostatic repulsions as explained in section 3.1. In contrast, for 66.7 kppm brines, a higher proportions of nanoparticle to surfactant increases the half-life dramatically (PECNP: Surfactant 4:6 in 66.7 kppm).

Table 5. Foam half decay time for variety of PECNP-Surfactant proportions (No half time: No recorded decay to half of the foam height due to stability of the foam system).

33.3 kppm System	half decay time (min)
Surfactant-$scCO_2$	65
PECNP:Surfactant-$scCO_2$ (3:7)	70
PECNP:Surfactant-$scCO_2$ (2:8)	80
PECNP:Surfactant-$scCO_2$ (1:9)	140
66.7 kppm System	**half decay time (min)**
Surfactant-$scCO_2$	No half time
PECNP:Surfactant-$scCO_2$ (4:6)	No half time
PECNP:Surfactant-$scCO_2$ (3:7)	No half time
PECNP:Surfactant-$scCO_2$ (2:8)	60
PECNP:Surfactant-$scCO_2$ (1:9)	30

Bubble rupture and CO_2-water lamella drainage occur in a longer period with lower rate, when PECNP forms ionic complexes with WLMs resulting in stronger electrostatic interactions in the lamella, including the plateau border and lamella border wall. In 66.7 kppm salinity brine, addition of PECNP to surfactant deteriorates the foam stability to some extent due to excessive charge attractions destabilizing the lamella (section 3.1). However, increasing the PECNP-surfactant solution ration (to PECNP of around 40 v/v %) provides a very stable lamella against lamella drainage, bubble coalescences and coarsening.

In foam fracturing, initial good film stability at initial stages is necessary, however, the generated foam needs to degrade when it comes to contact with oil, breaking, as fast during the flow back, leaving behind a fracture with high effective conductivity [3]. Therefore, an unstable lamella is required upon introduction of oil to foaming system. The foam stability measurements in the presence of oil are shown in Figure 7, where $scCO_2$ foam made in 33.3 kppm and 66.7 kppm was exposed to MLP crude oil in a view cell and the foam height with respect to time is shown.

The most stable foams presented in Figure 6 (with 1:9 and 4:6 PECNP:Surfactant ratios), are the least stable ones with fastest drainage when the oil is introduced to the view cell (Figure 7a, b).

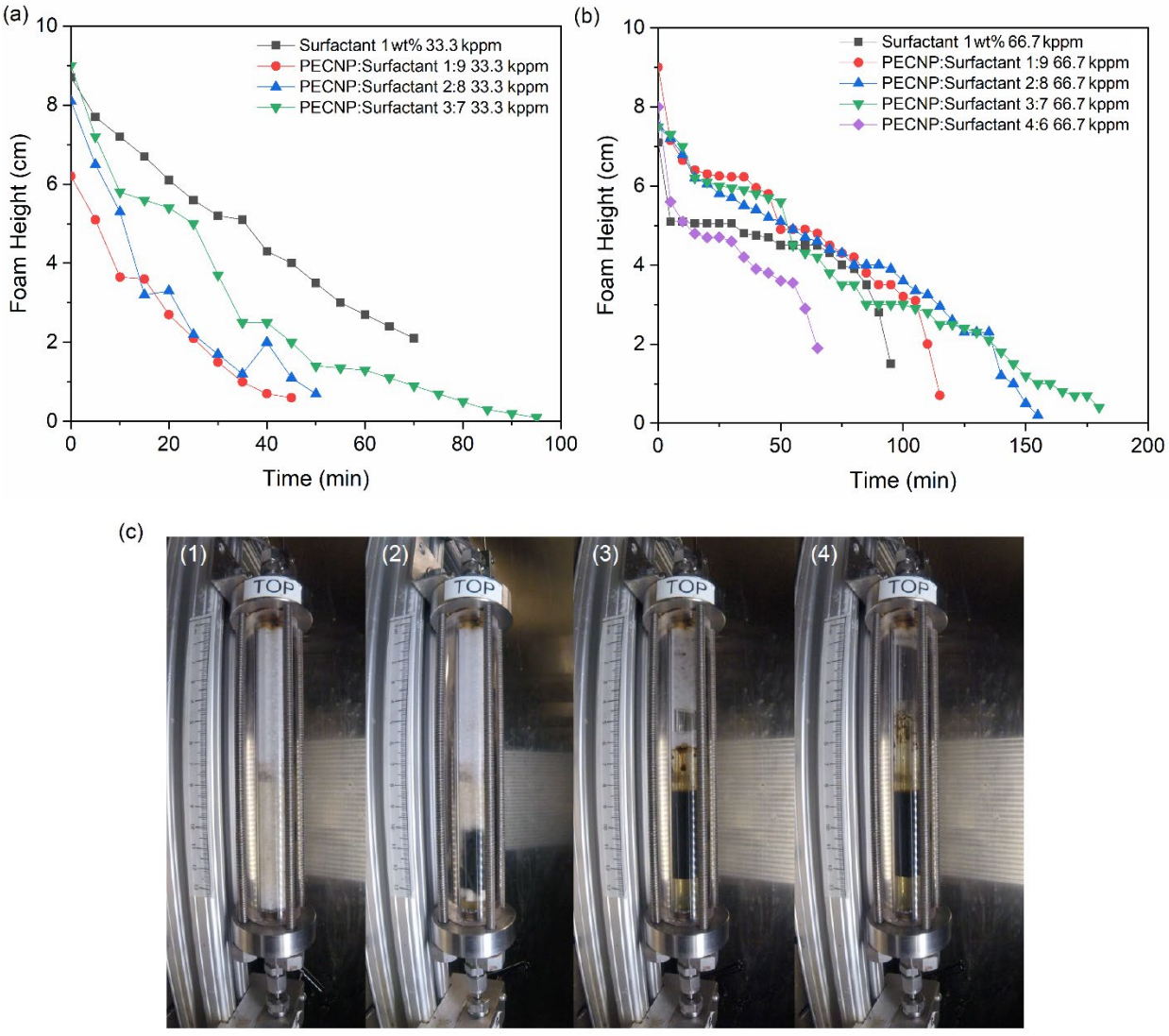

Figure 7. Foam stability measurements in the presence of crude oil for variety of PECNP-surfactant mixtures in 33.3 kppm brine solutions (b) 66.7 kppm brine solutions (c-1) Foam generation and isolation in the view cell (c-2) Introduction of the oil (c-3) Foam drainage in the presence of oil (c-4) Total foam disappearance and oil dominance

As it was previously noted, due to low interfacial tension between CO_2 and oil at high pressures, crude oil enters the original lamella, spreading and accelerating the thinning of lamella, coarsening the foam and causing gas bubble coalescence [47,48]. The time frame of the lamella

breakage depends heavily on the interaction of oil with the chemical components residing in the lamella, in this case, the PECNP-Surfactant complexes in lamella. As WLMs meet the oil molecules, the oil collapses into an emulsion [25]. The PECNP is also susceptible to degradations as carboxylic acid groups on MLP crude oil can trigger the secessions of coiled PEI-DS chains and electrostatic desorption of amine functional groups resulting in instability of the PECNP-WLMs in the lamella. Configuration of the oil at the gas-aqueous interface is another determining factor in oil instability, when pseudo-emulsion film formed between the oil and the gas is ruptured and oil spreads at the interface (bridge configuration) [40]. Accordingly, disintegration of the interface is anticipated due to positive entering and spreading coefficients previously reported by Xiao et al [49]. Table 6 summarizes the entering (E) and spreading (S) coefficients obtained by interfacial tension measurements as underlying equations for calculation are as following [50]:

(4) $$E = \sigma_{wg} + \sigma_{ow} - \sigma_{og}$$

(5) $$S = \sigma_{wg} - \sigma_{ow} - \sigma_{og}$$

Table 6. Entering and Spreading Coefficients for PECNP and Surfactant mixtures in the presence of $scCO_2$ and MLP crude oil

33.3 kppm System	σ_{wg}(mN/m)	σ_{ow}(mN/m)	E (mN/m)	S (mN/m)
Brine	33.42	11.47	44.89	21.95
Surfactant 1wt%	6.35	0	6.35	6.35
PECNP	14.97	0.87	15.84	14.1
PECNP:Surfactant (1:9)	6.43	0	6.43	6.43
66.7 kppm System	σ_{wg}(mN/m)	σ_{ow}(mN/m)	E (mN/m)	S (mN/m)
Brine	31.45	9.97	41.42	21.48
Surfactant 1wt%	6.55	0	6.55	6.55
PECNP	15.1	1.7	16.8	13.4
PECNP:Surfactant (4:6)	6.74	0	6.74	6.74

Surface tension between the oil and $scCO_2$ (σ_{og}) is considered a negligible value, since the operating condition is above the minimum miscibility pressure of the MLP and $scCO_2$ (MMP~ 1200 psi). Considering the positive values of E and S, crude oil is capable of entering the gas-water

interface and spreading on the liquid lamella, so the weakening of the disjoining pressure by disturbing the PECNP-Surfactant charge distribution and desorption to the lamella occurs spontaneously [49].

3.3. Bulk rheological properties. Hydraulic fracturing fluids experience high shear rates since fluid flows through the wellbore tubular and the shear rate drops significantly as the fluid gets into the fracture [51]. Therefore, shear rate sweep and static measurement studies help with understanding of the fluid behavior as fluid flow is mainly affected by flow geometry, time scale, foam microstructure and stability [52]. The rheology of dry CO_2 foam is widely regarded as non-Newtonian [52,53]. To characterize the non-Newtonian nature of $scCO_2$ foam created by the PECNP-surfactant mixture, first, the viscosity is measured at specific value of shear rate 2000 s^{-1} (Figure 8). The maximum apparent viscosity trend with time was observed for $scCO_2$ foam generated with PECNP:Surfactant systems with ratios of 1:9 and 4:6 prepared in 33.3 kppm and 66.7 kppm brines, respectively.

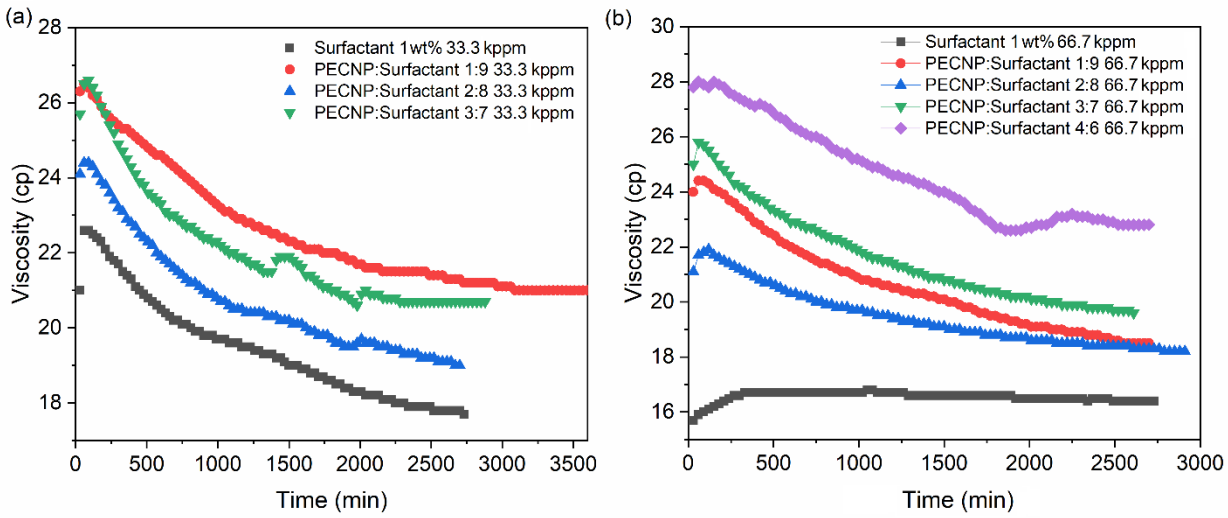

Figure 8. Viscosity with respect to time for 90% $scCO_2$ foam quality generated using 1:9, 2:8, 3:7 and 1:6 ratios of PECNP:Surfactant prepared in (a) 33.3 kppm and (b) 66.7 kppm brine. (Static Constant Shear Measurement)

It was previously noted that a high gas volume fraction above the volume fraction of bulk closed pack spheres can significantly increase the viscosity [54]. For the most stable mixtures (1:9 and 4:6), the bubble deformation at constant shear occurs with at a slower rate and the surface tension of PECNP at the interface restores the bubble shape. A higher apparent viscosity indicates the formation of smaller bubble sizes and a narrower size distribution as a result of monodispersed ordered structures formed by the PECNP stabilizers in the lamella. Higher shear resistivity originates from the ability of lamella to reverse the deformations as well as energy storage capacity at the interface controlled by chemical components at CO_2-water interface [52].

The shear thinning behaviors of PECNP-surfactants were examined with the shear rate sweep test shown in Figure 9. Shear thinning for WLM at high concentrations entangled with flexible polymer chains on the nanoparticle surface was reported due to alignment of wormlike chains, which increases the viscoelasticity of the mixture [25]. Wanniarachchi et al presented the effect of very low and very high viscosity fracture propagation and proppant transport [55]. Although high viscosity foam carries the required amount of proppants to the fracture, it may not be able to penetrate through micro-fractures with tiny openings, so the moderate viscosity range (50-250 cP) is recommended [55,56].

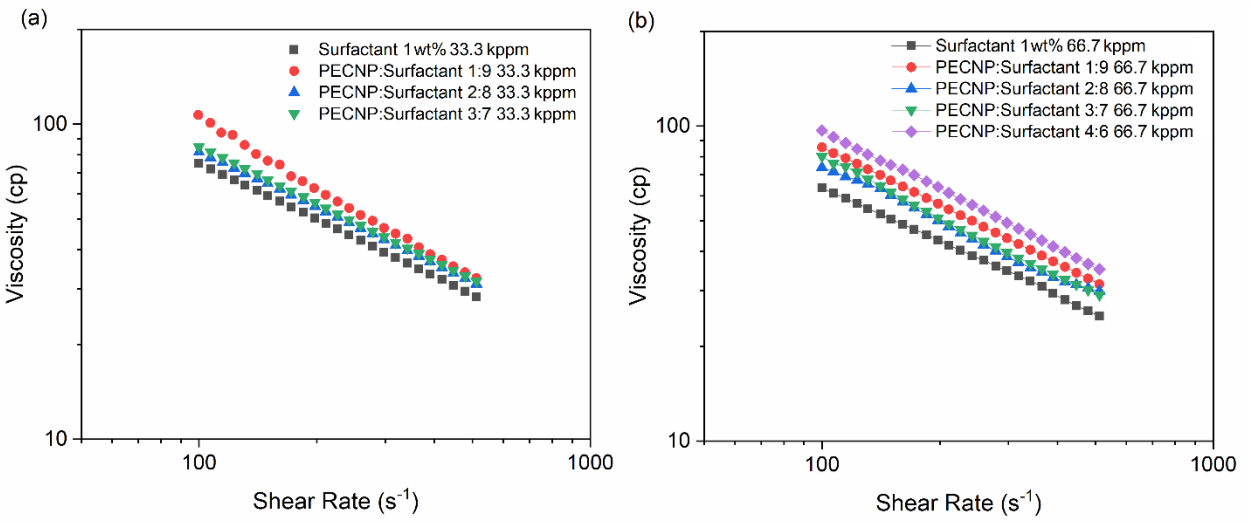

Figure 9. Viscosity with respect to shear rate of 90% scCO2 foam quality systems prepared using 1:9, 2:8, 3:7 and 4:6 ratios of PECNP:Surfactant in (a) 33.3 kppm and (b) 66.7 kppm brine. (Static Shear Sweep Measurement)

Shear thinning properties were evaluated through the laminar flow of incompressible $scCO_2$ foam through a Couette geometry rheometer and the results were matched by the power law model [52,57]. The apparent viscosity of the foam was reduced with increasing shear rate (shear softening with $n < 1$). Foam lamella drainage is at its lowest for the highest viscosities achieved with PECNP:Surfactant solutions with 1:9 ratio in 33.3 kppm and 4:6 in 66.7 kppm, respectively. Xue and coworkers demonstrated the viscous thick lamella's ability in 'CO_2- aqueous phase' to lower the rates of Ostwald ripening [22] which leads to generation of smaller bubbles [58]. The two PECNP-surfactant systems prepared in the 33.3 kppm and 66.7 kppm, respectively, offer higher apparent viscosity and flow consistency indices (Table 7) to enhance proppant transport and placement. Plastic deformation in the bulk fluid shown in Figure 9 are the result of stress induced bubble slide, coalescence and coarsening, which are controlled by elastic deformation of film containing a network of the PECNP-WLMs nanoparticles in the solid like interface studied by dilatational elasticity measurements (section 3.4).

Table 7. Flow consistency index (K) and flow behavior index (n) for variety of PECNP/Surfactant $scCO_2$ foam systems

33.3 kppm System	K (Pa s^n)	n
Surfactant-$scCO_2$	1184.3	0.402
PECNP:Surfactant-$scCO_2$ (3:7)	1387.9	0.394
PECNP:Surfactant-$scCO_2$ (2:8)	1261.6	0.407
PECNP:Surfactant-$scCO_2$ (1:9)	2916.4	0.276
66.7 kppm System	K (Pa s^n)	n
Surfactant-$scCO_2$	1035.7	0.368
PECNP:Surfactant-$scCO_2$ (4:6)	1683.1	0.380
PECNP:Surfactant-$scCO_2$ (3:7)	1443	0.371
PECNP:Surfactant-$scCO_2$ (2:8)	1163.9	0.405
PECNP:Surfactant-$scCO_2$ (1:9)	1464.6	0.385

As is observed in Table 7, the flow consistency index depicts the highest value for optimal concentrations of PECNP and WLMs, therefore, pressure drops across the tubular wellbore and fractures reaches their highest level for optimal values [59].

The formation of PECNPs as a result of electrostatic complexation of PECNP with WLMs helps to stabilize the water-CO_2 lamella by enhancing the viscosity, rigidity and electrostatic repulsion among lamellae surfaces [5]. In addition to Ostwald ripening slow down caused by high packing fractions of WLMs [22], association of surfactant with nanoparticle enhances the stability and viscosity of foam lamella even further.

3.4. Interfacial tension analysis and CMC. Figure 10 reveals the CMC calculations for a variety of surfactant concentrations in 33.3 kppm and 66.7 kppm brine systems according to the analysis of interfacial tension measurements. The determined CMCs are 0.059 wt% for 33.3 kppm brine and 0.055 wt% for 66.7 kppm brine. The presence of two charges on the surfactant molecule helps to form the micelles at lower concentrations [25]. Micellar solutions are formed above the CMC in both 33.3 kppm and 66.7 kppm high salinity brines. The zwitterionic surfactant micelles

were found to aggregate into worm like micelles (WLM) with self-assembly of surfactant into the elongated structures [25], thus, WLMs are expected to exist at 1wt% surfactant in high salinity brine. It was previously reported that salt ions would screen the electric double layer around the micelles and negatively affect the micellar assembly [40], however, the ionic activity of zwitterionic surfactant gives rise to the effective micellar volume fraction, therefore, CMC is still achieved at low concentrations.

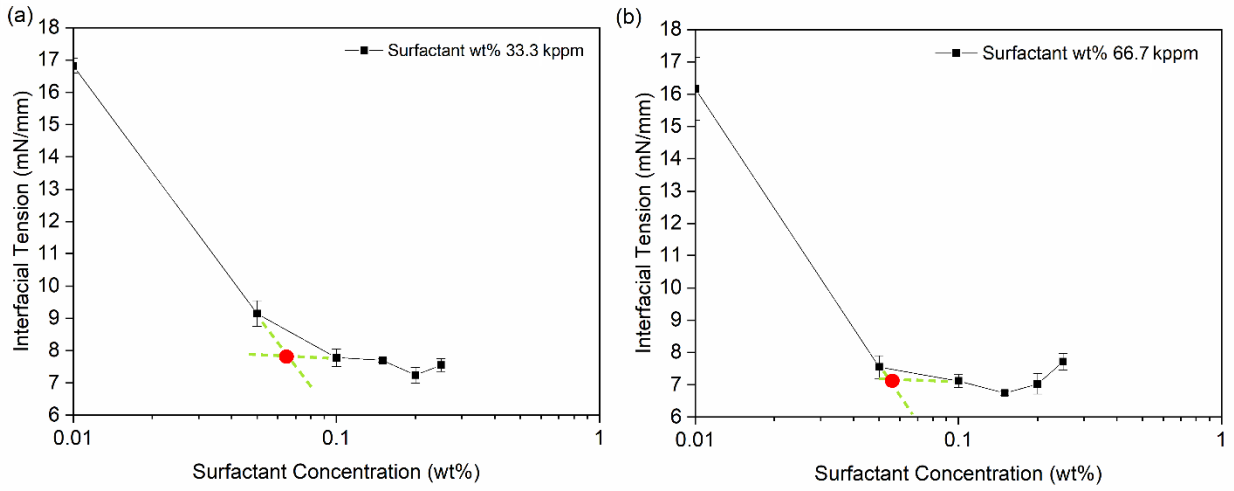

Figure 10. The critical micelle concentration for the viscoelastic surfactant at two different brine salinity of (a) 33.3kppm, and (b) 66.7kppm

Interfacial tension analysis results for $scCO_2$ bubbles formed in 1 wt% surfactant and PECNP in 33.3kppm and 66.7kppm brine systems suggest that the interfacial tension dramatically declines upon addition of surfactant and PECNP:Surfactant (Figure 11a,b). The very low IFT values of 5.4 and 6.4 mN/mm were obtained after addition of 1 wt% surfactant and PECNP-surfactant, with 1:9 ratio, to 33.3 kppm brine due to interfacial stabilization of $scCO_2$-brine lamella by improving repulsive forces created using ionic micelles, wormlike micellar self-assembly with PECNP and the network layer formed in the lamella. The IFT decline hits the minimum value (5.5

mN/mm) in lower concentration of ionic salts (33.3 kppm), whereas at higher concentrations (66.7 kppm), due to higher presence of ionic interactions and imbalanced forces, slightly a higher IFT value was detected. Addition of WLMs further stabilizes the $scCO_2$ lamella due to micellar branching and intra-aggregate attractions which lower the perturbations and imbalanced forces at the interface, as reported by Bouri and Tewes [39,60]. Polymeric nanoparticles present in the lamella in conjunction with WLMs form vesicular nano-capsules in which ionic aggregates reorient from the bulk phase to the lamella border and form arrays of stabilized PECNPs lining up on the interface between the supercritical phase and aqueous phase. While PECNPs don't necessarily reduce the IFT at the interface, one should note PECNP-surfactant nanoparticles are not a driving force for lamella instability and imbalanced forces at the interface, so the ionic compatibility and stability are preserved.

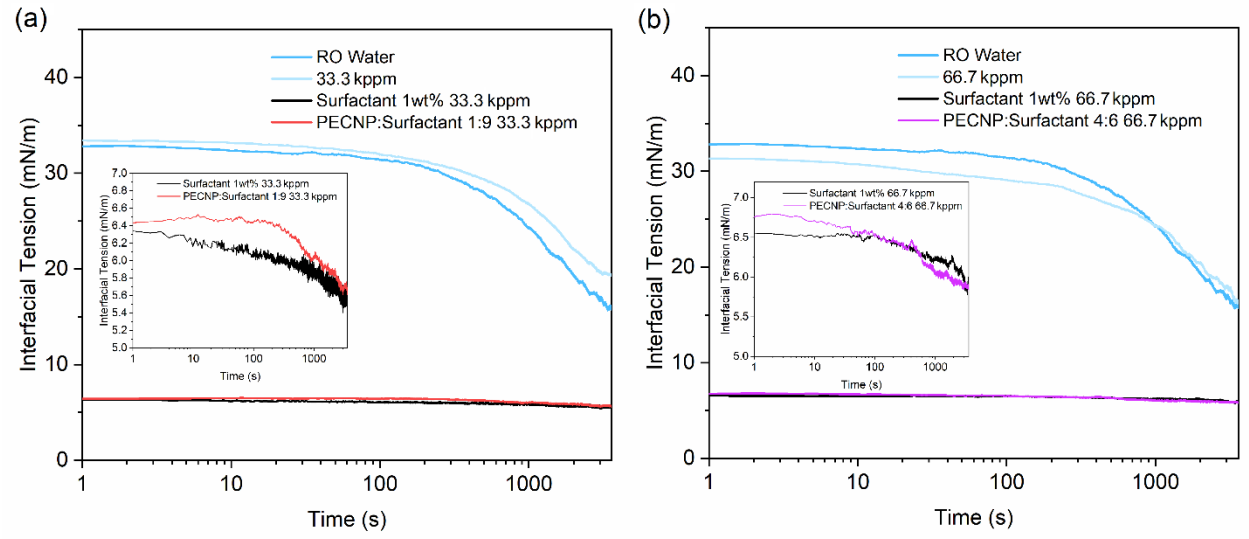

Figure 11. The interfacial tension measured for surfactant and PECNP in (a) 33.3kppm and (b) 66.7kppm brine

The dilatational elasticity was measured for RO water, surfactant and PECNP in (a) 33.3 kppm and (b) 66.7 kppm brine according to equation (1) using dynamic interfacial tension

measurements with $scCO_2$ (Figure 12). Dilatational elasticity represents the surface tension gradient which opposes the film drainage and provides a more stable film along the CO_2-water interface [40]. High values of surface elasticity does not guarantee the counterbalance of surfactant adsorption and surface diffusion to surface tension gradient and velocity of film thinning [40], thus the surface tension variation at the interface with respect to area change needs to fall within the allowable range to oppose the destabilizing forces [60,61].

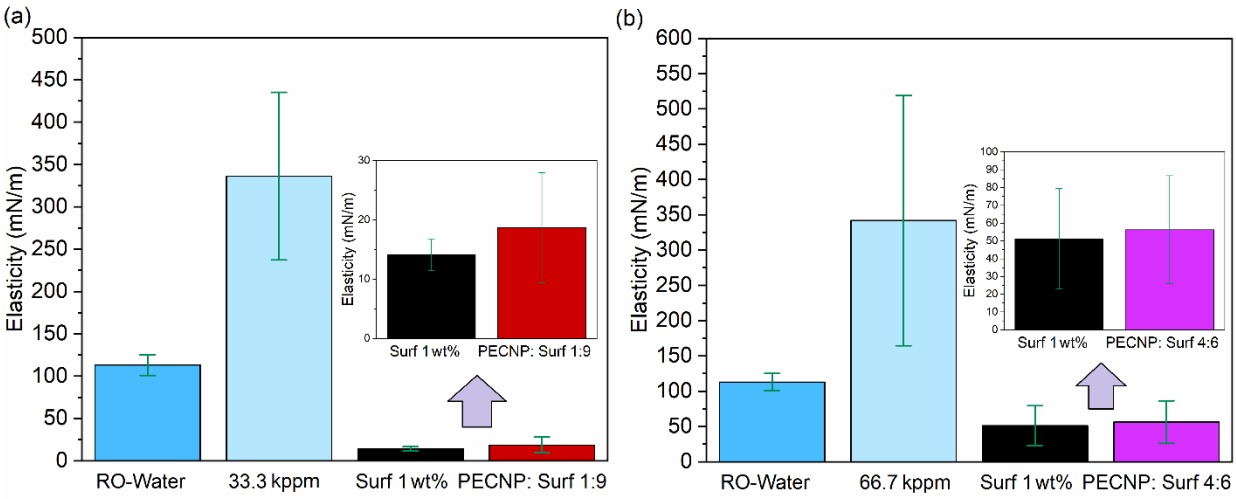

Figure 12. The dilatational elasticity measured for RO water and surfactant and PECNP in (a) 33.3kppm and (b) 66.7kppm brine according to interfacial tension analysis

Similar to IFT, the equilibrium surface dilatational elasticity is significantly lower than RO water and high salinity brines, when WLMs and PECNP-WLM mixtures exist in the CO_2-water interface (Figure 12). The difference between the elasticity obtained by WLMs and PECNP-WLM is not considerable, though addition of PECNP slightly increases the value as an indication of infinitesimal rigidity added to the interface, when PECNP-WLMs agglomerates form networks at the interface, giving rise to lamella elasticity and prolonging the bubble rupture time.

3.5. Transmission Electron Microscopy (TEM). Morphological representations of nanoparticles and surfactants in high salinity brines agree with the light scattering and Raman spectroscopy observations presented in sections 3.1 and 3.6. Figure 13 shows the TEM images for PECNP, 1wt% surfactants and PECNP-surfactant (with 1:9 ratio) prepared in 33.3 kppm high salinity brine. Formation of PECNPs as particles made by electrostatical interaction between PEI and DS is visible in Figure 13a, Figure 13b and Figure 13c. The size range of PECNPs is consistent with the predicted values of dynamic light scattering measurements (section 3-1). The 1wt% surfactant solution in the high salinity brine exhibits the formation of WLMs as elongated rod-like surfactant aggregates (Figure 13d, e and f).

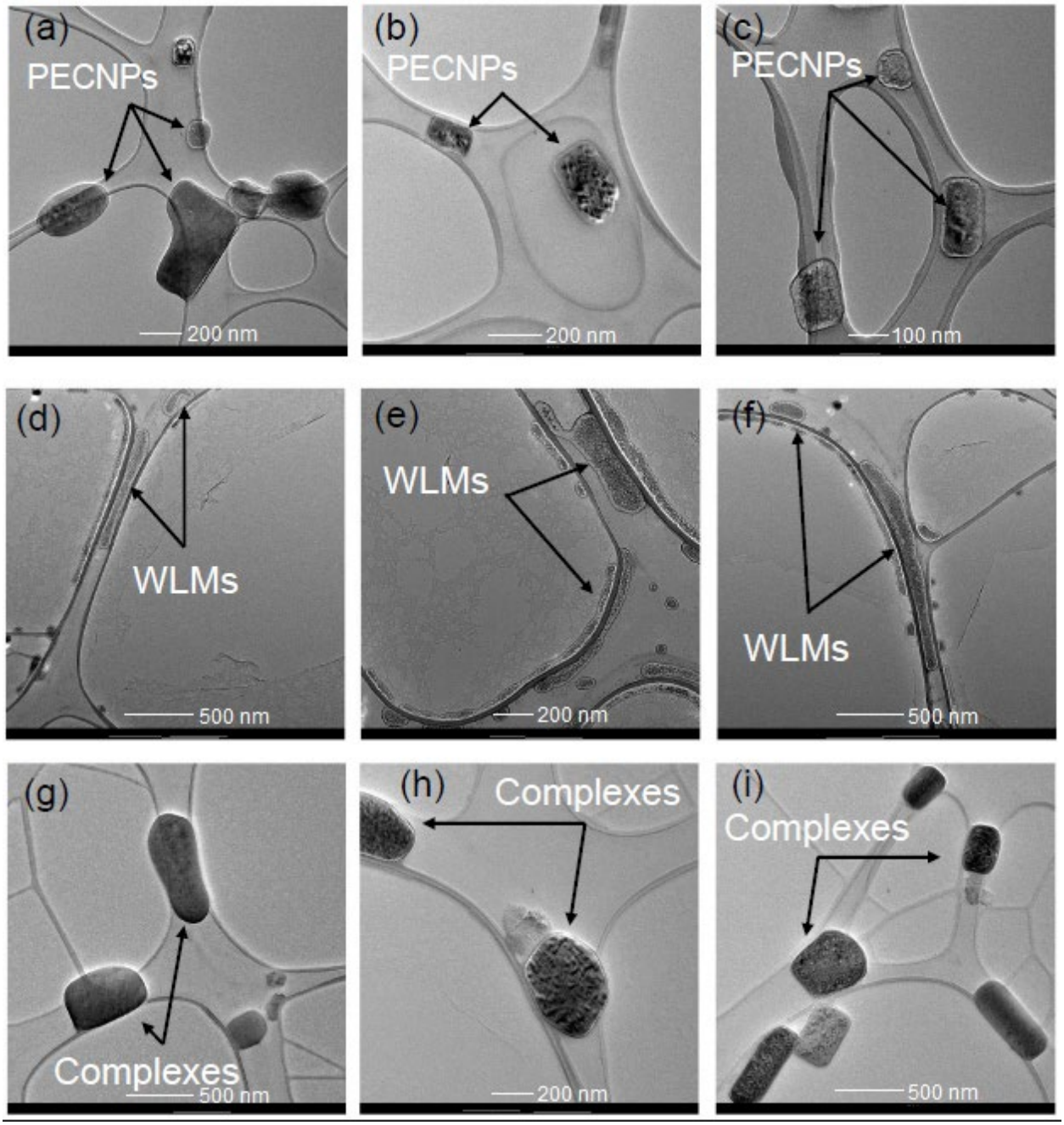

Figure 13. TEM images for PECNP nanoparticle (a, b and c), 1 wt% surfactant (d, e and f), and complexes of PECNP: Surfactant 1:9 (g, h and i) prepared in 33.3 kppm high salinity brine

Initially, nanoparticle agglomerates with WLMs form ring-like structures. WLMs are formed and coiled in the presence of nanoparticles starting to merge with the nanoparticle as they cover the outermost layer of a PECNP. Decoration of micelles on nanoparticle is derived through

the redistribution and direct adsorption of micelles on nanoparticles due to electrostatic attractions between the amine and sulfonate groups, confirmed by Raman spectroscopy (section 3.6). With time, the PECNP helps to form an elastic layer at the interface to overcome the foam coarsening, as, accumulation of elastic and positively charged hydrophilic particles at the plateau border hinders liquid drainage. Formation of stable nanogels in the form of vesicular structures (sphere to rod transition) was previously shown and studied in molecular dynamic simulations in cetyltrimethylammonium chloride (CTAC)-functionalized NP self-assembly [25,62], where double layer coverage of WLMs on oppositely charged and spherical nanoparticle induces the self-assembly of nanoparticle- surfactant in an aqueous medium.

3.6. Raman spectroscopy. Figure 14 illustrates the identified characteristic bands in Raman spectra and corresponding functional groups for the mixtures of PECNP and 1 wt% surfactant prepared in 33.3 kppm brine.

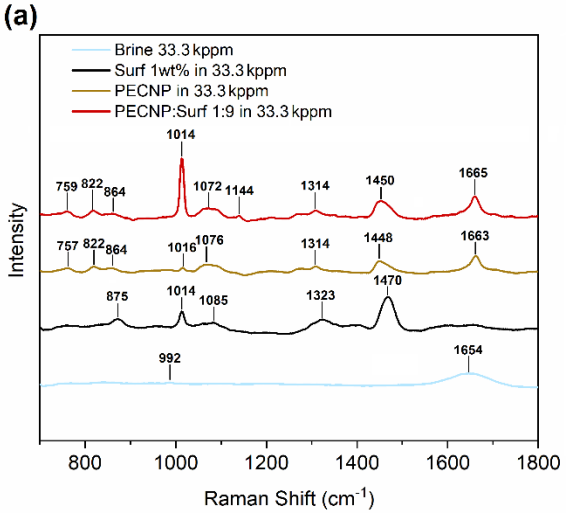

(b)

Raman shift (cm^{-1})	Vibrational mode/Assignment
992 (free, aqueous) 1014 (bound)	$\nu_1 SO_4$
600-1300	νC-C (aliphatic chain vibrations)
1200-1340	δN-H (Amide III) νC-N stretch
1400-1470	δCH_2, δCH_3 asym
1510-1580	νC-N, δN-H (Amide II)
1640	δH_2O
1680-1820	δN-H (Amide I) νC=O

Figure 14. The identified bands and corresponding assignments in Raman spectra for 33.3 kppm brine, surfactant, PECNP, and PECNP:surfactant (1:9) in brine (a) and identification of key Raman bands (b) corresponding groups based on the values reported in the literature [63,64]

The PECNP and surfactant spectra share many of the same bands, corresponding to their backbones and other shared functional groups. Of special note are the 1014 cm^{-1} and 1665 cm^{-1}

bands. The first represents a totally symmetric sulfate stretching mode associated with the surfactant (present to a very minor extent in the PECNP spectrum due to the dextran sulfate used to make the PECNP), while the second band represents the δN-H in plane bending generated by the nitrogen-hydrogen bonds and is unique to the polyehtyleneimine. A band around 1654 cm^{-1} is observed in the brine (and underlying some of the other spectra) that can be attributed to the remaining water present in the lyophilized samples [65,66]. The 33.3 kppm brine spectrum has a weak band for free sulfate (SO_4^{-2}) from Na_2SO_4 centered at 992 cm^{-1}[67]. The chemically bound sulfate band can be found at 1014 cm^{-1} in the three other spectra as that functional group is found in both the surfactant and the dextran sulfate used to make the PECNPs, although the relative intensity of this band varies significantly among the spectra. This observed shift is consistent with previously reported findings by Wang and coworkers [68] about the noticeable band shift for SO_4^{2-} band from 992 to 1010 cm^{-1} in titanium hydroxide complexation with sulfate.

In order to better understand the changes in intensity of the sulfate signal, especially in the PECNP-surfactant spectrum, a simple model was developed. Using least-squares fitting, four PECNP:Surfactant 1:9 Raman spectra (collected from different locations within the lyophilized samples) were fit with average PECNP and surfactant spectra. The contribution of the PECNP and surfactant spectra to the PECNP-surfactant is reported in the text box for each spectrum. These numbers are purely mathematical and as such they reflect concentration that have not been calibrated for quantitative analysis. The residual of corresponding fit indicates locations within the spectra where the PECNP:Surfactant spectrum is not completely explained by the sum of the components. If the PECNP:Surfactant spectrum represented a mixture, rather than a change in chemistry, then its residual should represent the noise in the data, however, this is clearly not the case, as shown in Figure 15. In each residual, the sulfate band at 1014 cm^{-1} stands out as

significantly different, indicating that complexation between the PECNP and the surfactant occurs and that the complex itself has a unique Raman signature (possibly due to a change in chemical environment of the key functional groups). The strength of the sulfate band varies between samples, however, as the complexes are not homogenous, this should not be a surprise. There are other minor changes to peaks within the Raman spectrum, particularly at 1144 cm^{-1}, indicating that the changes due to complexation are not confined to the polyatmic anions.

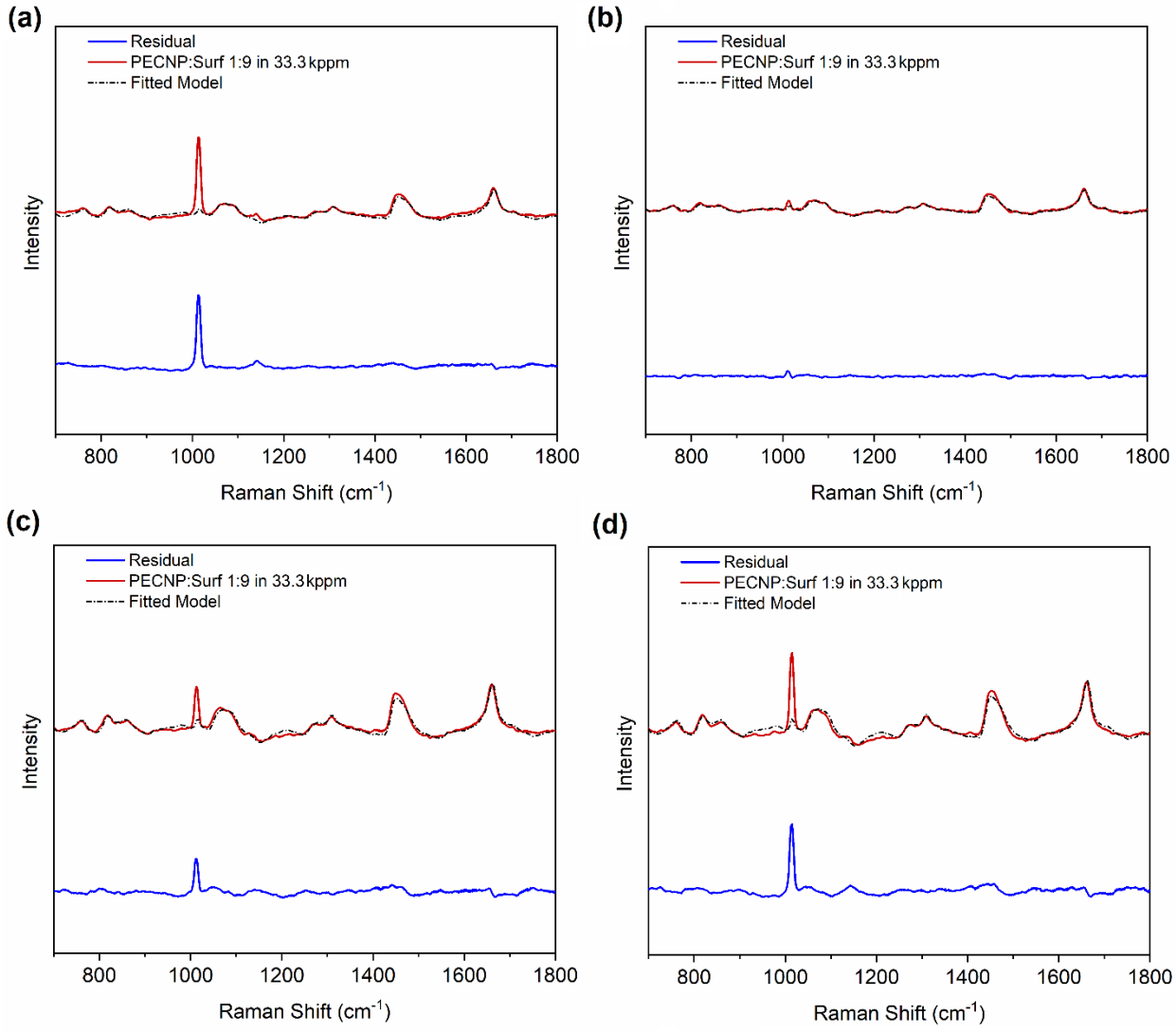

Figure 15. The Raman spectra of four PECNP:surfactant 1:9 samples (blue) fit with average PECNP and surfactant spectra for surfactant (red dots) and corresponding residual (black, offset) along with zero residual line (also black, offset).

Taken together the IR spectra (figure S2), Raman data the surfactant structure resembles the amidopropyl hydroxysultaine with a long hydrophobic tail, sulfonate and quaternary ammonium pendant groups. The main functional groups are quaternary and secondary amines as well as pendant hydroxide groups, amide and sulfonate ($R\text{-}SO_3^-$). Combination of ammonium and sulfonate offers a zwitterionic surfactant with both cationic and anionic charge head groups capable of conjunction with PECNP in $scCO_2$ lamella interface.

3.7. Dynamic Fluid Loss. It is critical to control the leak off rate of fracturing fluids to reduce pumping cost and to ensure the mechanical integrity of the formation. Production from horizontal wells in tight reservoirs requires high internal fracture conductivity since conductivity provides a path to accommodate high velocity hydrocarbon flow [69]. Fluid loss coefficients were measured with the setup presented in Figure 3 for the $scCO_2$ foams prepared with highest apparent and dynamic viscosities (1:9 ratio and 4:6 ratio of PECNP- surfactant in 33.3 kppm and 66.7 kppm brine systems, respectively) and the results are shown in Figure 16.

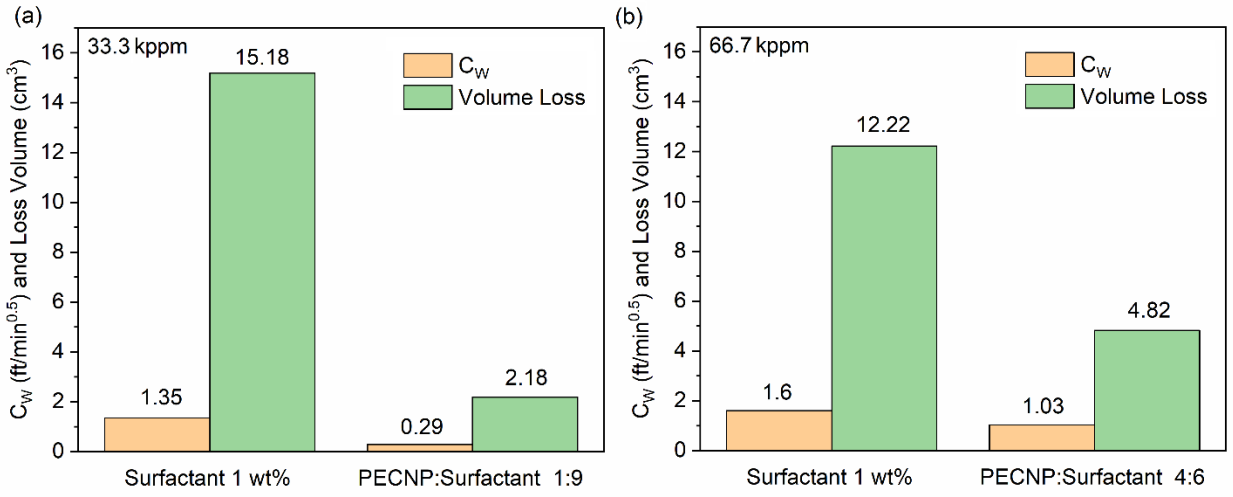

Figure 16. Total fluid loss (gas and liquid) and fluid loss coefficient for the mixtures prepared in (a) 33.3kppm and (b) 66.7kppm high salinity brines.

The initial and final permeability of a Kentucky sandstone tight core exposed to the flow of $scCO_2$ foam with PECNP-surfactant remained constant (0.18 mD) revealing minimal pore throat plugging and damage to the core as a result of core exposure to the fracturing fluid. The fluid loss volume and fluid loss coefficients were significantly lowered when PECNP-surfactant was used as the aqueous component of the foaming solution as compared to surfactant alone, resulting in a reduced leaked volume in the tight core and enhanced fracture properties. The fluid loss coefficient is a function of core permeability, surfactant/PECNP concentration and temperature [70]. Furthermore, it was previously reported that higher foam quality provides higher viscosity and reduced leak-off [71]. Efficient merge of WLMs to PECNPs resulted in the formation of nanoparticles performing as fluid loss additives during the injection of the foam solutions. Higher apparent viscosity achieved as a result of adding PECNP to the solutions, leads to reduced formation damage due to lower rate of fluid clean up [70]. The results were consistent with rheological measurements where PECNP-surfactant systems prepared in 33.3 kppm and 66.7 kppm brine exhibited the highest viscosities over the shear thinning period. It was previously argued that osmotic pressure, which leads to foam tendency to retain water, prevents the water leak-off to the formation [72], thus, it can be concluded that PECNP-WLMs enhance the proppant carrying capability of $scCO_2$ foam while lowering the water usage .

3.8. Sand Pack Measurements. The detailed flooding scenarios and mobility features in the sand pack experiment are indicated in Table 6. The permeability of the pack after an initial brine flood with 33.3 kppm and 66.7 kppm brine varies between 144 to 170 D, based on Darcy's law, the value represents the high permeability porous pack (SI). The apparent viscosity of fracturing fluid in the pack is calculated according to the Darcy's equation (equation 4):

(4) $$\mu_{app} = \frac{k.A.\Delta P.}{Q.L}$$

where k is permeability of the fluid inside the pack, ΔP is the pressure difference between the two ends of the pack, A is the cross section area of the pack, Q is the volumetric flow rate of fracturing fluid flow in the pack column and L is the pack length. Accordingly, the apparent viscosity is obtained and the results are shown in Table 8.

Table 8. Flood scenarios and mobility features for surfactant, oil and $scCO_2$ foam floods in the sand pack

Sand pack scenarios	PV (cm^3)	Q (cm^3/s)	k (D)	ΔP (psi)	μ_{app} (cP)
33.3kppm Brine Flood	7.58	0.1	169.94	0.38	0.93
Oil Flood	7.58	0.1	169.94	2.71	6.66
Surf 1wt% $scCO_2$ Flood	7.58	0.1	169.94	6.00	14.75
Secondary Brine Flood	7.58	0.1	154.22	0.32	0.71
33.3kppm Brine Flood	7.63	0.1	154.23	0.48	1.07
Oil Flood	7.63	0.1	154.23	2.42	5.4
PECNP:Surf 1:9 $scCO_2$ Flood	7.63	0.1	154.23	8.43	18.8
Secondary Brine Flood	7.63	0.1	157.77	0.35	0.8
66.7kppm Brine Flood	7.41	0.1	155.14	0.56	1.26
Oil Flood	7.41	0.1	155.14	2.87	6.44
Surf 1wt% $scCO_2$ Flood	7.41	0.1	155.14	4.02	9.02
Secondary Brine Flood	7.41	0.1	156.12	0.34	0.77
66.7kppm Brine Flood	7.47	0.1	154.91	0.43	0.96
Oil Flood	7.47	0.1	154.91	2.66	5.96
PECNP:Surf 4:6 $scCO_2$ Flood	7.47	0.1	154.91	5.56	12.46
Secondary Brine Flood	7.47	0.1	143.87	0.36	0.75

Upon oil saturation, 10 pore volumes of crude oil was flooded to completely saturate the pack. The efficiency of the oil flood varied between 84 to 100%. Consequently, the $scCO_2$ foam was flooded to clean up the oil saturated pack. Foam breakthrough occurred at 5.9 and 5.35 PV of foam flood for 33.3 kppm and 66.7 kppm brines, respectively, representing the better oil clean-up and sweep efficiency for 33.3 kppm salinity $scCO_2$ foams as a result of the foam half decay time and higher viscosity shown in Table 5 and Table 7.

The pressure drop is recorded during the propagation of oil or $scCO_2$ foam through the sand pack. Figure 17a, b exhibits the magnitude of the pressure drop with respect to time of foam flood. Relative stability, propagation and performance of the $scCO_2$ foam in the pack helped to effectively mobilize and recover the crude oil in the fractured reservoirs. Accordingly, large

effective viscosities and sufficient mobility control for PECNP-Surfactant enhanced $scCO_2$ foam are concluded.

The saturation of oil and water phase in the pack after the oil flood is calculated from the following sets of equations:

(5) $$S_{o1} = \frac{V_{oi} - V_{oc} - V_{P2} - V_{P1}}{PV} \text{ and}$$

(6) $$S_{w1} = 1 - S_{o1},$$

where S_{o1} is the oil saturation in the pack, V_{oi} is the injected volume of oil through the lines and pack, V_{oc} is the collected volume of oil in the outlet after the oil flood. V_{P1} and V_{P2} are purt volumes of inlet and outlet lines connected to the pack. S_{w1} is the remaining saturation of aqueous phase in the pack. PV is pore volume of ceramic proppants in the pack. Likewise, the saturation of oil and water phase in the pack after the foam flood is shown as:

(7) $$S_{o2} = S_{o1} - \frac{V_{ocf} - V_{P2} - V_{P1}}{PV} \text{ and}$$

(8) $$S_{w1} = 1 - S_{o2},$$

where S_{o2} and V_{ocf} are the oil saturation and collected oil volume.

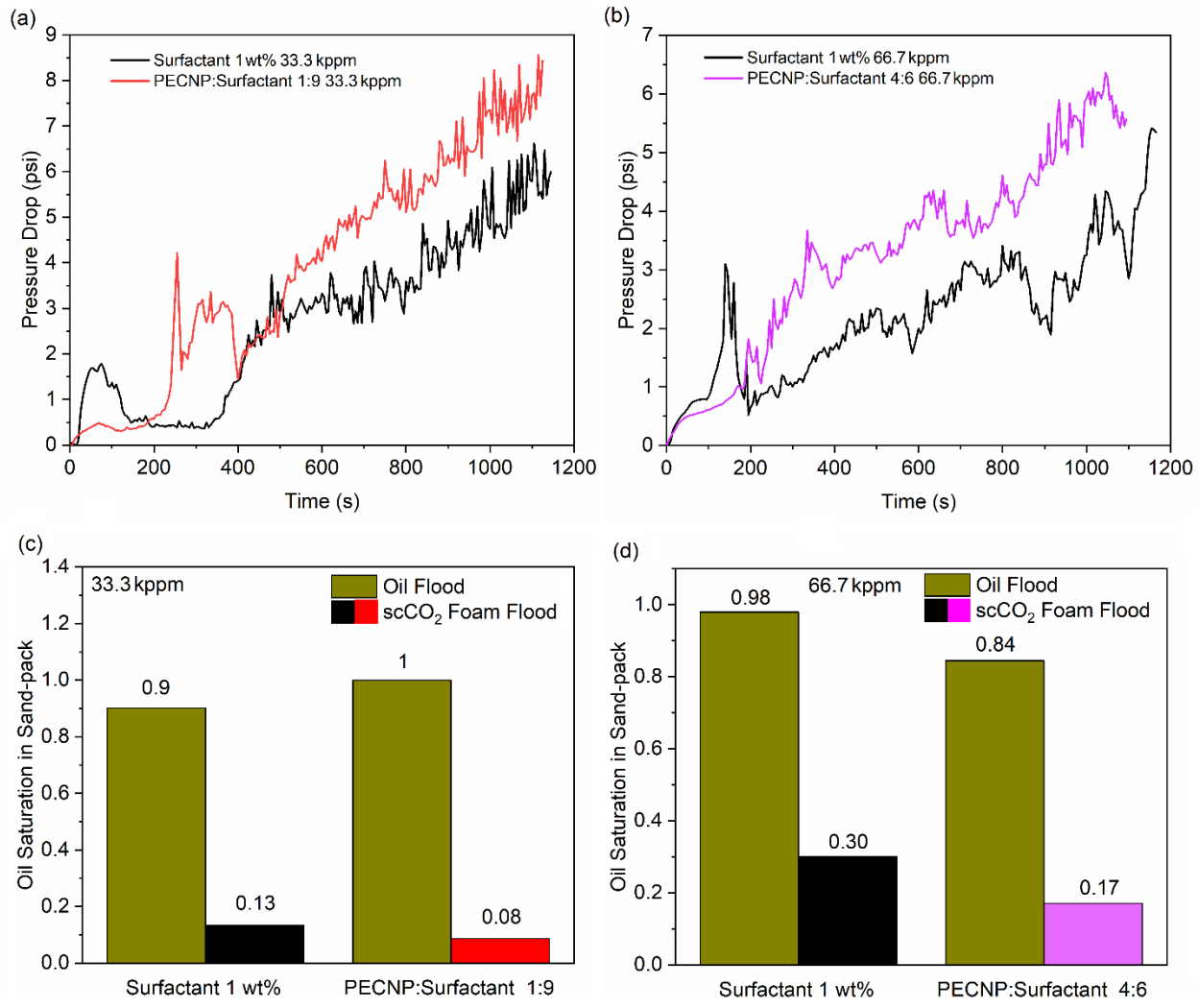

Figure 17. Foam pressure drop and saturation profile for $scCO_2$ foams generated by surfactant and PECNP-surfactants in high salinity brine. (a) Pressure drop profile for foam flood inside the oil saturated sand pack in 33.3 kppm brine (b) Pressure drop profile for foam flood inside the oil saturated sand pack in 66.7 kppm brine (c) Oil saturation in sand pack after oil flood and foam flood for clean-up in 33.3 kppm brine (d) Oil saturation in sand pack after oil flood and foam flood for clean-up

The oil saturation is measured before and after foam flood with 1 wt% surfactant and PECNP-surfactant enhanced $scCO_2$ foam is shown in Figure 17c, d. The initial oil saturation varies between 0.84 to 1 depending on the available pore volume and packing efficiency. The secondary oil saturation drops to lower values after performing the surfactant foam flood indicating capability of the foam to clean-up the pack. Efficiency of the clean-up improves with 1:9 and 4:6 PECNP-

surfactant $scCO_2$ foam as oil saturation drops 85 % to 92 % reduction in 33.3 kppm systems (Figure 17c) and 69 % to 86 % in 66.7 kppm systems (Figure 17d). The results are consistent with the shear and apparent viscosities presented in Figure 8 and Figure 9 where 1:9 and 4:6 ratios exhibit the capacity for clean-up and oil improvement of sweep efficiency. It is concluded that enhanced viscosity as a result of bulk foam stability using PECNP-surfactant improves the dynamics of foam flow in porous media.

4. CONCLUSIONS

Herein, we reported the results for a responsive $scCO_2$ foam which combines improved viscosity and stability to carry proppants as well as instability in the presence of the oil phase, resulting in rapid degradation upon contact. A novel mixture containing PECNP-surfactant in high salinity brine was successfully prepared to enhance $scCO_2$ foam, reduce formation damage and improve clean-up properties during the hydraulic fracturing process. The major conclusions can be summarized as follows:

1. The presented mixture overcomes the traditional issues with of water-based foam liquids such as foam instability at high temperature and pressure, in addition to formation damage due to high water content. It offers a perfect compatibility of $scCO_2$ with high salinity produced waters (divalent ions) up to 67 kppm TDS (higher than sea level) to minimize the amount of fresh water use and produced water disposal in the hydraulic fracturing process, helping to create a sustainable process of oil recovery from tight shale formations and to store large volumes of CO_2 from the atmosphere.

2. Minimum polyelectrolyte and surfactant concentrations are required for effective performance with the recommended PECNP-surfactant mixture. A zwitterionic surfactant resistant to high temperatures, compatible with high salinity brine and charged nanoparticles was employed

to interact with PECNPs electrostatically. The mixture lowers the surface tension of $scCO_2$ bubbles up to 74 % in 33.3 kppm and 93 % in 66.7 kppm high salinity brines.

3. The formation of vesicular complexes as a result of electrostatic complexation of PECNP with WLMs was visually identified with TEM images and confirmed with Raman and spectroscopic. The ionic complexes are capable of stabilizing the water-CO_2 lamella by enhancing the viscosity (rheometry), rigidity (dilatational elasticity) and electrostatic repulsion (zeta potential measurements) among lamellae surfaces. A least-square fitting algorithm as morphological model proved the synergistic complexation between PECNP and surfactant based on fitting analysis on acquired Raman spectra from ionic mixtures. The underlying mechanism was identified as electrostatic rearrangement of WLMs along the structure of PECNP to form electrostatically bond layers with nanoparticles and create a stable complex.

4. The stability of $scCO_2$ bubbles are improved through the formation of electrostatically enhanced bubble s containing the aggregates of PECNP-surfactant. The foam stability drastically improved in view cell test as optimum mixtures presented longer foam life time. PECNP-surfactant mixtures represent a new prospect for stabilizing the bubble film in a high salinity environment and the tailoring the lamella repulsive forces through addition of different ratios of PECNP to surfactant to overcome the lamella drainage and film thinning.

5. Fluid loss commonly occurs in fracturing process can be controlled using the presented PECNP-surfactant $scCO_2$ foam. Bot h fluid loss volume and fluid loss coefficients for CO_2 and water were lowered up to 86 and 78% respectively, by employing PECNP- surfactant resulting in lower formation damage.

6. Rapid and easy clean-up is offered by PECNP-surfactant $scCO_2$ foam when the high pressure drop and decline in oil saturation was detected in sand pack tests.

ASSOCIATED CONTENT

Supporting Information (SI) is provided by the authors. A brief explanation of experimental procedures, functional characterization of surfactant, process flow diagram for air foam stability setup, and supplementary physical property measurement for PECNP and PECNP/Surfactant mixtures, additional dilatational elasticity and sand pack calculations as well as supplementary data for Raman spectroscopy are presented in SI.

AUTHOR INFORMATION

Corresponding author

*Reza Barati Ghahfarokhi, Department of Chemical and Petroleum Engineering, The University of Kansas, Lawrence, Kansas 66045, E-mail: rezab@ku.edu

Phone Number: (785)864-1232

ORCID

Hooman Hosseini: 0000-0002-5072-6737

Jyun Syung Tsau: 0000-0002-1497-1911

Karen Shafer-Peltier: 0000-0002-0610-8990

Craig Marshall: 0000-0002-9468-7266

Qiang Ye: 0000-0002-2143-9173

Reza Barati Ghahfarokhi: 0000-0002-1064-9562

Author Contribution

The manuscript was written through contributions of all authors. All authors have given approval to the final version of the manuscript.

ACKNOWLEDGMENT

The authors are grateful to the National Science Foundation (#123350) for providing financial support. The project is funded by National Science Foundation EPSCor Research Infrastructure Improvement Program: Track -2 Focused EPSCoR Collaboration award (OIA- 1632892). Authors acknowledge Harcros Chemicals for providing the surfactant used in this work. Authors also extend their appreciation to Dr. Cory J, Berkland, Matthew Christopher and Stephanie Johnson in the Pharmaceutical Chemistry Department at University of Kansas (KU) for their generous help in freeze drying of samples, Dr. Qiang (Charles) Ye for his support with FTIR and Raman spectroscopic measurements performed at Institute for Bioengineering Research (IBER) Laboratories at University of Kansas and Carson Rufledt for Raman spectroscopy analysis in the KU Department of Geology. The endeavors of Zach Kessler, Jeff Worth and Scott Ramskill from Chemical and Petroleum Engineering department and Tertiary Oil Recovery Program (TORP) at the University of Kansas are appreciated. Last but not the least, the authors gratefully acknowledge Dr. Prem S. Thapa from KU Microscopy and Analytical Imaging Laboratory for the help with Transmission Electron Microscopy analysis.

Abbreviations

$scCO_2$, supercritical CO_2; CCUS, carbon capture utilization and storage; VES, viscoelastic surfactant; WLM, wormlike micelle; PEI, polyethylenimine; DS, dextran sulfate; PECNP, polyelectrolyte complex nanoparticle; MLP, Mississippian limstone play; RO-DI water, reverse osmosis and deionized water; CMC, critical micelle concentration; FTIR, Fourier transform Infrared spectroscopy; MMP, minimum miscibility pressure; TEM, transmission electron microscopy; IFT, interfacial tension; TDS, total dissolved solids.

REFERENCES

[1] Scanlon BR, Reedy RC, Nicot JP. Comparison of water use for hydraulic fracturing for

unconventional oil and gas versus conventional oil. Environ Sci Technol 2014;48:12386–93. doi:10.1021/es502506v.

[2] Smith, M.B., Montgomety CT. Hydraulic Fracturing. Taylor & Francis Group; 2015. doi:10.1016/B978-0-12-409547-2.11013-3.

[3] Hosseini H, Tsau J, Barati R. SPE-189555-MS Lowering Fresh Water Usage in Hydraulic Fracturing by Stabilizing $scCO_2$ Foam with Polyelectrolyte Complex Nanoparticles Prepared in High Salinity Produced Water 2018.

[4] Yekeen N, Padmanabhan E, Idris AK. A review of recent advances in foam-based fracturing fluid application in unconventional reservoirs. J Ind Eng Chem 2018. doi:10.1016/j.jiec.2018.05.039.

[5] Al-muntasheri GA, Advanced E, Aramco S. Nanoparticle-Enhanced Hydraulic-Fracturing Fluids : A Review. SPE Prod Oper Conf Exhib 2017;32:187–95.

[6] US Environmental Protection Agency - US EPA. Hydraulic Fracturing for Oil and Gas: Impacts from the Hydraulic Fracturing Water Cycle on Drinking Water Resources in the United States (Main Report - EPA/600/R-16/236fa) 2016:666.

[7] Clifford PJ, Mellor DW, Jones TJ. Water Quality Requirements for Fractured Injection Wells. Corrosion 1991.

[8] Gross SA, Avens HJ, Banducci AM, Tvermoes BE, Panko JM. Surface Spills in Hydraulic Fracturing Operations and Recommendations for Safety Management 1 2013;63:424–32.

[9] Carter K, Hammack R, Hakala J. Hydraulic Fracturing and Organic Compounds-Uses, Disposal and Challenges. SPE East Reg Meet 2013. doi:10.2118/165692-MS.

[10] Gupta DVS, Company BJS. SPE 119424 Unconventional Fracturing Fluids for Tight Gas Reservoirs 2009:19–21.

[11] Gupta DVS, Carman PS, Hughes B. Associative Polymer System Extends the Temperature Range of Surfactant Gel Frac Fluids. SPE Interational Symp Oilf Chem 2011;SPE 141260:1–8.

[12] Alajmi MD, Mahsoon AH, Al-hajri NM, Aramco S. Feasibility Study of Utilizing Hydraulic Turbines to Recover Excess Power 2016:1–6.

[13] Ribeiro L, Sharma MM. A New Three-Dimensional, Compositional, Model for Hydraulic Fracturing with Energized Fluids. SPE Annu Tech Conf Exhib 2012:8–10. doi:10.2118/159812-MS.

[14] Qajar A, Xue Z, Worthen AJ, Johnston KP, Huh C, Bryant SL, et al. Modeling fracture propagation and cleanup for dry nanoparticle-stabilized-foam fracturing fluids. J Pet Sci Eng 2016;146:210–21. doi:10.1016/j.petrol.2016.04.008.

[15] Rezaei F, Lawson S, Hosseini H, Thakkar H, Hajari A, Monjezi S, et al. MOF-74 and UTSA-16 film growth on monolithic structures and their CO_2 adsorption performance. Chem Eng J 2017;313:1346–53. doi:10.1016/j.cej.2016.11.058.

[16] Kang D, Lee MG, Jo H, Yoo Y, Lee SY, Park J. Carbon capture and utilization using industrial wastewater under ambient conditions. Chem Eng J 2017;308:1073–80. doi:10.1016/j.cej.2016.09.120.

[17] Barati R, Liang JT. A review of fracturing fluid systems used for hydraulic fracturing of oil and gas wells. J Appl Polym Sci 2014;131:1–11. doi:10.1002/app.40735.

[18] Gandossi L. An overview of hydraulic fracturing and other formation stimulation technologies for shale gas production. 2013. doi:10.2790/99937.

[19] Rochelle C a., Moore Y a. The solubility of supercritical CO_2 into pure water and synthetic Utsira porewater. Br Geol Surv Comm Rep CR/02/052 2002:28.

[20] Nguyen VH, Kang C, Roh C, Shim J-J. Supercritical CO_2 -Mediated Synthesis of CNT@Co_3O_4 Nanocomposite and Its Application for Energy Storage. Ind Eng Chem Res 2016;55:7338–43. doi:10.1021/acs.iecr.5b04069.

[21] Barbati AC, Desroches J, Robisson A, McKinley GH. Complex Fluids and Hydraulic Fracturing. Annu Rev Chem Biomol Eng 2016;7:415–53. doi:10.1146/annurev-chembioeng-080615-033630.

[22] Xue Z, Worthen AJ, Da C, Qajar A, Ketchum IR, Alzobaidi S, et al. Ultradry Carbon Dioxide-in-Water Foams with Viscoelastic Aqueous Phases. Langmuir 2016;32:28–37. doi:10.1021/acs.langmuir.5b03036.

[23] Breward CJW, Howell PD. The drainage of a foam lamella. J Fluid Mech 2002;458:379–406. doi:10.1017/S0022112002007930.

[24] Osei-Bonsu K, Shokri N, Grassia P. Foam stability in the presence and absence of hydrocarbons: From bubble- to bulk-scale. Colloids Surfaces A Physicochem Eng Asp 2015;481:514–26. doi:10.1016/j.colsurfa.2015.06.023.

[25] Dreiss CA, Feng Y. Wormlike Micelles. The Royal Society of Chemistry; 2017. doi:10.1039/9781782629788.

[26] William JKM, Ponmani S, Samuel R, Nagarajan R, Sangwai JS. Effect of CuO and ZnO

nanofluids in xanthan gum on thermal, electrical and high pressure rheology of water-based drilling fluids. J Pet Sci Eng 2014;117:15–27. doi:10.1016/j.petrol.2014.03.005.

[27] Vryzas Z, Mahmoud O, Nasr-El-Din HA, Kelessidis VC. Development and Testing of Novel Drilling Fluids Using Fe_2O_3 and SiO_2 Nanoparticles for Enhanced Drilling Operations. Int Pet Technol Conf 2015. doi:10.2523/IPTC-18381-MS.

[28] Cai J, Chenevert ME, Sharma MM, Friedheim JE. Decreasing Water Invasion Into Atoka Shale Using Nonmodified Silica Nanoparticles. SPE Drill Complet 2012;27:103–12. doi:10.2118/146979-PA.

[29] Haroun M, Hassan S, Ansari A, Kindy N, Sayed N, Ali B, et al. Smart Nano-EOR Process for Abu Dhabi Carbonate Reservoirs. Abu Dhabi Int Pet Exhib Conf 2012:1–13. doi:10.2118/162386-MS.

[30] Wang J, Xue G, Tian B, Li S, Chen K, Wang D, et al. Interaction between surfactants and SiO2nanoparticles in multiphase foam and its plugging ability. Energy and Fuels 2017;31:408–17. doi:10.1021/acs.energyfuels.6b02592.

[31] Zeng S, Zhang X, Bai L, Zhang X, Wang H, Wang J, et al. Ionic-Liquid-Based CO_2 Capture Systems: Structure, Interaction and Process. Chem Rev 2017;117:9625–73. doi:10.1021/acs.chemrev.7b00072.

[32] Hosseini H, Dornbusch DA, Suppes GJ. Improved Electrochemical Performance of Alkaline Batteries Using Quaternary Ammonia Polysulfone-Functionalized Separators. Ind Eng Chem Res 2016;55:8557–66. doi:10.1021/acs.iecr.5b04930.

[33] Chen M, Shafer-Peltier K, Randtke SJ, Peltier E. Competitive association of cations with

poly(sodium 4-styrenesulfonate) (PSS) and heavy metal removal from water by PSS-assisted ultrafiltration. Chem Eng J 2018;344:155–64. doi:10.1016/j.cej.2018.03.054.

[34] Veisi M, Johnson S, Shafer-Peltier K, Liang JT, Berkland C, Chen M, et al. Controlled release of poly(vinyl sulfonate) scale inhibitor to extend reservoir treatment lifetime. J Appl Polym Sci 2018;47225:1–11. doi:10.1002/app.47225.

[35] Anandan R, Johnson S, Barati R. SPE-187489-MS Polyelectrolyte Complex Stabilized CO_2 Foam Systems for Hydraulic Fracturing Application 2017:1–19.

[36] Nazari N, Tsau J-S, Barati R. CO_2 Foam Stability Improvement Using Polyelectrolyte Complex Nanoparticles Prepared in Produced Water. Energies 2017;10:516. doi:10.3390/en10040516.

[37] Kalyanaraman N, Arnold C, Gupta A, Tsau JS, Ghahfarokhi RB. Stability improvement of CO2 foam for enhanced oil-recovery applications using polyelectrolytes and polyelectrolyte complex nanoparticles. J Appl Polym Sci 2017;134:1–15. doi:10.1002/app.44491.

[38] Veisi M, Johnson S, Peltier K, Berkland C, Liang J-T, Barati R. Application of polyelectrolyte complex nanoparticles to increase the lifetime of poly vinyl sulfonate scale inhibitor. Proc - SPE Int Symp Form Damage Control 2018;2018–Febru.

[39] Tewes F, Pierre M, Boury F. Dynamical and Rheological Properties of Fluorinated Surfactant Films Adsorbed at the Pressurized CO_2 - H_2O Interface 2011:8144–52.

[40] Schramm LL. Foams: Fundamentals and Applications in the Petroleum Industry. American Chemical Society; 1994. doi:10.1021/ba-1994-0242.

[41] Shafer-Peltier KE, Haka AS, Fitzmaurice M, Crowe J, Myles J, Dasari RR, et al. Raman

microspectroscopic model of human breast tissue: Implications for breast cancer diagnosis in vivo. J Raman Spectrosc 2002;33:552–63. doi:10.1002/jrs.877.

[42] Howard GC, Fast CR. Optimum Fluid Characteristics for Fracture Extension. Drill Prod Pract 1957.

[43] CARBO Ceramics Inc, CARBOECONOPROP low density ceramic proppant n.d. https://www.carboceramics.com/Oil-gas/Fracture-technologies/ceramic-proppant/carboeconoprop-low-density (accessed October 10, 2018).

[44] Whitfill D. Lost Circulation Material Selection, Particle Size Distribution and Fracture Modeling with Fracture Simulation Software. IADC/SPE Asia Pacific Drill Technol Conf Exhib 2008:1–12. doi:10.2118/115039-MS.

[45] Denkov ND, Ivanov IB, Kralchevsky PA, Wasan DT. A possible mechanism of stabilization of emulsions by solid particles. J Colloid Interface Sci 1992;150:589–93. doi:10.1016/0021-9797(92)90228-E.

[46] Zhang XL, Penfold J, Thomas RK, Tucker IM, Petkov JT, Bent J, et al. Adsorption behavior of hydrophobin and hydrophobin/surfactant mixtures at the air-water interface. Langmuir 2011;27:11316–23. doi:10.1021/la201706p.

[47] Lau H, O'Brien S. Effects of spreading and nonspreading oils on foam propagation through porous media. SPE Reserv Eng 1988:893–6. doi:10.2118/15668-PA.

[48] Kuhlman M. Visualizing the Effect of Light Oil in CO2 Foams. J Pet Technol 1990;42. doi:https://doi.org/10.2118/17356-PA.

[49] Xiao S, Zeng Y, Vavra ED, He P, Puerto M, Hirasaki GJ, et al. Destabilization , Propagation

, and Generation of Surfactant- Stabilized Foam during Crude Oil Displacement in Heterogeneous Model Porous Media 2018. doi:10.1021/acs.langmuir.7b02766.

[50] Ross S. Inhibition of Foaming. II1,2A Mechanism for the Rupture of Liquid Films by Antifoaming Agents. J Phys Colloid Chem 1950;54:429–36. doi:10.1021/j150477a018.

[51] Dreiss CA, Feng Y. (RSC soft matter series 6) Wormlike micelles_advances in systems, characterisation and applications-Royal Society of Chemistry (2017).pdf. 2017.

[52] Faroughi SA, Pruvot AJCJ, McAndrew J. The rheological behavior of energized fluids and foams with application to hydraulic fracturing: Review. J Pet Sci Eng 2018;163:243–63. doi:10.1016/j.petrol.2017.12.051.

[53] Xiao C, Balasubramanian SN, Clapp LW. Rheology of Viscous CO_2 Foams Stabilized by Nanoparticles under High Pressure. Ind Eng Chem Res 2017;56:8340–8. doi:10.1021/acs.iecr.7b01404.

[54] Alzobaidi S, Lotfollahi M, Kim I, Johnston KP, Dicarlo DA. Carbon Dioxide-in-Brine Foams at High Temperatures and Extreme Salinities Stabilized with Silica Nanoparticles 2017:10680–90. doi:10.1021/acs.energyfuels.7b01814.

[55] Wanniarachchi WAM, Ranjith PG, Perera MSA, Lashin A, Al Arifi N, Li JC. Current opinions on foam-based hydro-fracturing in deep geological reservoirs. Geomech Geophys Geo-Energy Geo-Resources 2015;1:121–34. doi:10.1007/s40948-015-0015-x.

[56] Zhang J. Chemical Engineering III. London: CRC Press.; 2014.

[57] Lauridsen J, Twardos M, Dennin M. Shear-Induced Stress Relaxation in a Two-Dimensional Wet Foam. Phys Rev Lett 2002;89:1–4. doi:10.1103/PhysRevLett.89.098303.

[58] Szabries M, Jaeger P, Amro MM. Foam Analysis at Elevated Pressures for Enhanced Oil Recovery Applications. Energy & Fuels 2019:acs.energyfuels.8b03088. doi:10.1021/acs.energyfuels.8b03088.

[59] Dlugogorski BZ, Schaefer TH, Kennedy EM. Verifying Consistency of Effective-Viscosity and Pressure- Loss Data for Designing Foam Proportioning Systems. Natl Inst Stand Technol 2005;3.

[60] F. Boury, T. Ivanova, I. Panaieotov, J. E. Proust, A. Bois and JR. Dilatational Properties of Adsorbed Poly(D,L-lactide) and Bovine Serum Albumin Monolayers at the Dichloromethane/Water Interface. Langmuir 1995;11:1636–44.

[61] Georgieva D, Cagna A, Langevin D. Link between surface elasticity and foam stability. Soft Matter 2009;5:2063–71. doi:10.1039/b822568k.

[62] Sambasivam A, Sangwai A V., Sureshkumar R. Self-Assembly of Nanoparticle-Surfactant Complexes with Rodlike Micelles: A Molecular Dynamics Study. Langmuir 2016;32:1214–9. doi:10.1021/acs.langmuir.5b03689.

[63] Long DA. Infrared and Raman characteristic group frequencies. Tables and chartsGeorge Socrates John Wiley and Sons, Ltd, Chichester, Third Edition. vol. 35. 2004. doi:10.1002/jrs.1238.

[64] Raman data and analysis. HORIBA JOBIN YVON Inc n.d. http://www.horiba.com/fileadmin/uploads/Scientific/Documents/Raman/bands.pdf.

[65] Roessl U, Leitgeb S, Pieters S, De Beer T, Nidetzky B. In situ protein secondary structure determination in ice: Raman spectroscopy-based process analytical tool for frozen storage

of biopharmaceuticals. J Pharm Sci 2014;103:2287–95. doi:10.1002/jps.24072.

[66] Kumar S, Verma T, Mukherjee R, Ariese F, Somasundaram K, Umapathy S. Raman and infra-red microspectroscopy: Towards quantitative evaluation for clinical research by ratiometric analysis. Chem Soc Rev 2016;45:1879–900. doi:10.1039/c5cs00540j.

[67] Ben Mabrouk K, Kauffmann TH, Aroui H, Fontana MD. Raman study of cation effect on sulfate vibration modes in solid state and in aqueous solutions. J Raman Spectrosc 2013;44:1603–8. doi:10.1002/jrs.4374.

[68] Wang W, Liu Y, Xue T, Li J, Chen D, Qi T. Mechanism and kinetics of titanium hydrolysis in concentrated titanyl sulfate solution based on infrared and Raman spectra. Chem Eng Sci 2015;134:196–204. doi:10.1016/j.ces.2015.05.006.

[69] Saldungaray P, Palisch T. Hydraulic fracture optimization in unconventional reservoirs. World Oil 2012:7–13.

[70] Harris PC. Dynamic Fluid-Loss Characteristics of CO_2-Foam Fracturing Fluids. SPE Prod Eng 1987:89–94.

[71] Fei Y, Johnson RL, Gonzalez M, Haghighi M, Pokalai K. Experimental and numerical investigation into nano-stabilized foams in low permeability reservoir hydraulic fracturing applications. Fuel 2018;213:133–43. doi:10.1016/j.fuel.2017.10.095.

[72] Ribeiro LH, Sharma MM. Multiphase Fluid-Loss Properties and Return Permeability of Energized Fracturing Fluids. Spe Prod Oper 2012;27:265–77. doi:10.2118/139622-PA.

Nomenclature

φ	gas volume fraction
$\Delta\pi_e$	equilibrium part of surface pressure variation (mN/m)
$\Delta\pi_{ne}$	non equilibrium part of surface pressure variation (mN/m)
E_e	equilibrium surface dilatational elasticity (mN/m)
U_b	velocity of compression (m/s)
A_i	initial surface area (m^2)
t	time (s, min)
τ	relaxation time (s)
V_L	fluid loss volume (cm^3)
C_w	fluid loss coefficient ($ft/min^{1/2}$)
S_P	Spurt volume (cm^3)
σ_{wg}	water-gas surface tension (mN/m)
σ_{ow}	oil-water surface tension (mN/m)
σ_{og}	oil-gas surface tension (mN/m)
E	entering coefficient (mN/m)
S	spreading (mN/m)
μ_{app}	apparent viscosity of fluids (cP)
ΔP	pressure difference between the two ends of the pack (psi)
A	cross section area of the pack (cm^2)
Q	volumetric flow rate of fracturing fluid flow (cm^3/s)
L	pack length (cm)
PV	pore volume (cm^3)
k	permeability (D)
S_o	saturation of oil in the pack
S_w	saturation of water in the pack
V_o	volume of oil in the pack (cm^3)
V_{P1}	volume of inlet lines to the pack (cm^3)
V_{P2}	volume of lines in outlet of the pack (cm^3)
V_{oc}	collected volume of oil in the outlet after oil flood (cm^3)
V_{ocf}	collected volume of oil in the outlet after foam flood (cm^3)
K	flow consistency index ($Pa.S^n$)
n	flow behavior index
η	viscosity (cP)
$\dot{\gamma}$	shear rate (s^{-1})

Graphical Abstract:

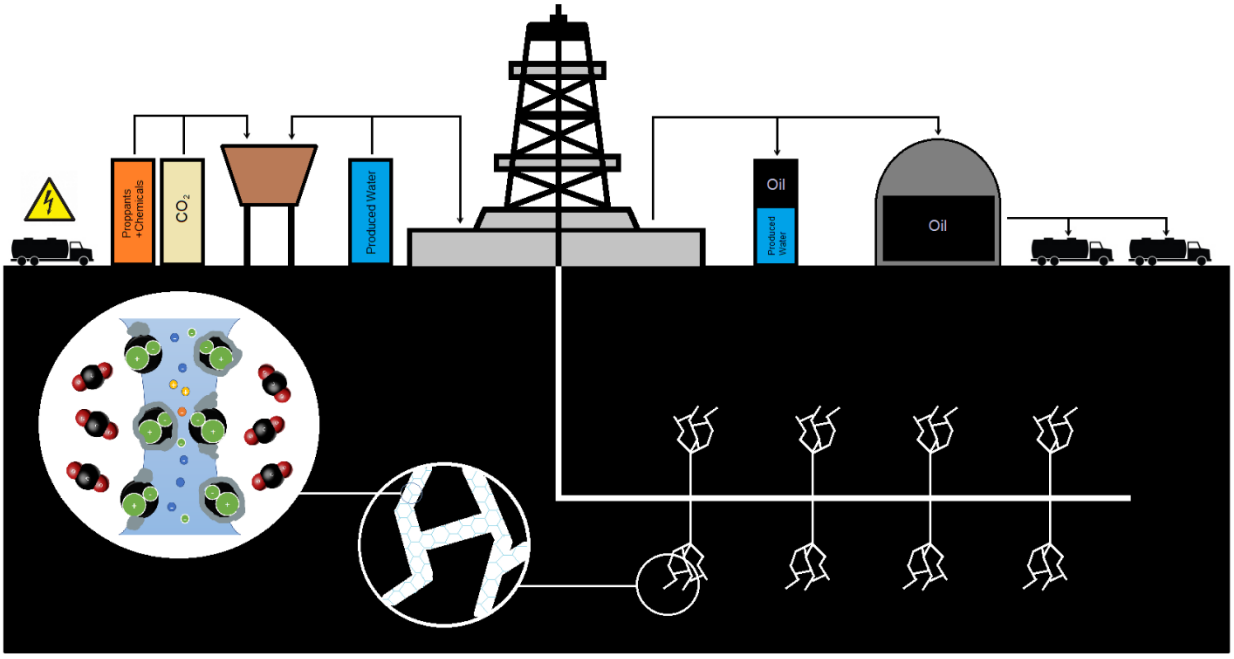

Unconventional oil recovery with $scCO_2$ foam fluids stabilized by PECNP/Surfactant at the lamella interface is the subject of this work. The presented mixture reduces the amount of fresh water usage and produced water disposal to the surface in hydraulic fracturing process.